International Journal of Heat and Mass Transfer 77 (2014) 1231–1249

Contents lists available at ScienceDirect

International Journal of Heat and Mass Transfer

journal homepage: www.elsevier.com/locate/ijhmt

Micro-channel evaporator for space applications – 2. Assessment of predictive tools

Hyoungsoon Lee [a], Ilchung Park [a], Issam Mudawar [a,*], Mohammad M. Hasan [b]

[a] Purdue University Boiling and Two-Phase Flow Laboratory (PU-BTPFL), School of Mechanical Engineering, 585 Purdue Mall, West Lafayette, IN 47907, USA
[b] NASA Glenn Research Center, 21000 Brookpark Road, Cleveland, OH 44135, USA

ARTICLE INFO

Article history:
Received 29 January 2014
Received in revised form 2 June 2014
Accepted 3 June 2014
Available online 1 July 2014

Keywords:
Flow boiling
Micro-channel
Pressure drop
Flow orientation
Reduced gravity

ABSTRACT

This study is the second part of a two-part study addressing the effectiveness of micro-channel evaporators for space applications. The first part provided pressure drop and heat transfer data for FC-72 that were acquired with a test module containing 80 of 231 μm wide × 1000 μm deep micro-channels. The tests were performed in three flow orientations: horizontal, vertical upflow and vertical downflow over broad ranges of mass velocity and heat flux. The present part uses these experimental results to assess the accuracy of published predictive tools. The two-phase heat transfer coefficient data are compared to predictions of 15 popular correlations, and pressure drop data to 7 mixture viscosity relations used in conjunction of the Homogeneous Equilibrium Model (*HEM*), and 18 correlations based on the Separated Flow Model (*SFM*). These models and correlations are carefully assessed in pursuit of identifying the most accurate tools. In addition, three important criteria for implementing micro-channel flow boiling in space systems are proposed: avoiding large pressure drop, avoiding critical heat flux (CHF), and negating the influence of body force. It is shown that micro-channels require significantly smaller mass velocities to negate body force effects than macro-channels, and are therefore very effective for space applications.

1. Introduction

Pressure drop and heat transfer characteristics of single-phase micro-channel heat sinks have been the subject of extensive study spanning three decades, especially in conjunction with electronics cooling [1–6]. Aside from their very compact and lightweight design, these heat sinks provide unprecedented enhancement in heat transfer coefficient. Their thermal attributes are readily recognized for laminar flow, where the heat transfer coefficient is inversely proportional to hydraulic diameter. This implies the high heat transfer coefficient can be increased simply by decreasing hydraulic diameter. The advantages of utilizing a small diameter are also achieved with turbulent flow. But because these heat sinks rely on sensible heat rise of the coolant for heat dissipation, they typically incur large temperature gradients in both coolant and device being cooled.

This shortcoming is largely responsible for shifting focus in recent years from single-phase to two-phase micro-channel heat sinks. With phase change, far greater heat transfer coefficients are achieved by capitalizing upon the coolant's sensible and latent heat rather than sensible heat alone. This helps greatly reduce coolant flow rate when dissipating the same amount of heat as from a single-phase heat sink, let alone the reduction in coolant inventory for the cooling system at large. Reliance on latent heat exchange also enables two-phase heat sinks to achieve superior temperature uniformity.

For several decades, flow boiling has been examined in predominantly macro-channel geometries as well as a variety of cooling configurations, including pool boiling [7–10], channel flow boiling [11–13], jet [14–17] and spray [18–21], as well as enhanced surfaces [22–24]. Despite many similarities between the boiling phenomena associated with these different configurations, extending this understanding to flow boiling in micro-channels is by no means straightforward. Because of small hydraulic diameter, bubble nucleation, departure and coalescence are far more influenced by surface tension and wall confinement effects than macro-channels. These influences have a profound effect on two-phase regime transitions, pressure drop, heat transfer coefficient and critical heat flux (CHF).

This paper is the second part of a two-part study concerning the influence of orientation on pressure drop and heat transfer

* Corresponding author. Tel.: +1 (765) 494 5705; fax: +1 (765) 494 0539.
E-mail address: mudawar@ecn.purdue.edu (I. Mudawar).
URL: https://engineering.purdue.edu/BTPFL (I. Mudawar).

http://dx.doi.org/10.1016/j.ijheatmasstransfer.2014.06.008
0017-9310/

Nomenclature

b	constant in Eq. (13)
Bd	Bond number
Bo	Boiling number
C_c	contraction coefficient
c_p	specific heat at constant pressure
D_h	hydraulic diameter
E	coefficient in two-phase heat transfer coefficient correlations
f	Fanning friction factor
F_q	fraction of wall heat flux consumed in converting near-wall liquid to vapor
Fr	Froude number
G	mass velocity
g	gravitational acceleration
g_n	component of gravity normal to heated wall
H	mean thickness of phase layer
h	heat transfer coefficient
H_b	distance between upper and lower thermocouples
H_{ch}	height of micro-channel
H_p	height of inlet/outlet plenums
H_t	distance between bottom wall of micro-channel and upper thermocouple
k	thermal conductivity
L	length; length of micro-channel
M	molecular weight
m	fin parameter
$\dot{m}$	mass flow rate for single micro-channel
N_{ch}	number of micro-channels
N_{conf}	confinement number
Nu	Nusselt number
q''	heat flux
q''_{eff}	effective heat flux based on width of unit cell containing single micro-channel
q''_m	critical heat flux based on heated perimeter
P	pressure, perimeter
ΔP	pressure drop
P_R	reduced pressure
Pr	Prandtl number
Re	Reynolds number
S	suppression coefficient in two-phase heat transfer coefficient correlations
Su	Suratman number
T	temperature
U	mean velocity of phase layer
v	specific volume
W_{ch}	width of single micro-channel
We	Weber number
W_p	width of inlet/outlet plenums
W_W	width between micro-channels
X	Lockhart–Martinelli parameter
x_e	thermodynamic equilibrium quality
X_{tt}	Lockhart–Martinelli parameter for turbulent liquid and turbulent vapor flows
z	stream-wise coordinate
z_0	axial location where vapor layer velocity just exceeds liquid layer velocity
z^*	axial location parameter in Eq. (13)

Greek Symbols

α	void fraction
β	aspect ratio of micro-channel (W_{ch}/H_{ch})
δ	vapor layer thickness
η	fin efficiency
θ	flow orientation angle from horizontal flow, percentage predicted within ±30%
λ_c	critical wavelength
μ	dynamic viscosity
ξ	percentage predicted within ±50%
ρ	density
σ	surface tension
σ_c	contraction ratio
ϕ	two-phase pressure drop multiplier

Subscripts

A	accelarational
b	bottom thermocouple plane
c	contraction
cb	convective boiling
ch	micro-channel
cir	circumferential
d	developing
e	expansion
exp	experimentally-determined
F	frictional, wetted
f	liquid, bulk fluid
fd	fully-developed
fo	liquid only
G	gravitational
g	vapor
H	heated
nb	nucleate boiling
$pred$	predicted
s	solid
sat	saturated
sc	subcooled boiling
sp	single-phase
sub	subcooling
t	top thermocouple plane
tot	total
tp	two-phase
w	wall

associated with flow boiling in micro-channels. This study is part of NASA's Flow Boiling and Condensation Experiment (FBCE), which is projected for deployment in the International Space Station (ISS) in 2017. In part 1 [25], the pressure drop and heat transfer characteristics were examined experimentally for horizontal flow, vertical upward and vertical downflow for different mass velocities and orientations. The micro-channel module consists of 80 parallel 231 μm wide × 1000 μm deep micro-channels, and operating conditions are provided in Table 1. This part will assess predictive tools for pressure drop and heat transfer coefficient in pursuit of identifying the most accurate tools. Also discussed are criteria for negating the influence of body force when implementing the micro-channel heat sink in reduced gravity space systems.

2. Assessment of heat transfer correlations

2.1. Heat transfer data reduction

As discussed in part 1 of this study [25], the local heat transfer coefficient is calculated by applying energy balance to the control volume of a unit cell consisting of a single micro-channel and

Table 1
Operating conditions of present study.

	Horizontal		Vertical upward		Vertical downward	
	Pressure drop	Heat transfer	Pressure drop	Heat transfer	Pressure drop	Heat transfer
G (kg/m^2 s)	155.9–792.0	196.6–792.0	151.5–834.5	259.2–834.5	175.4–772.3	175.4–772.3
G/ρ_f (m/s)	0.10–0.50	0.13–0.50	0.10–0.53	0.17–0.53	0.11–0.49	0.11–0.49
q''_{eff} (W/cm^2)	2.19–9.46	3.10–9.41	2.14–9.56	3.43–9.56	2.47–9.89	3.28–9.30
P_{in} (kPa)	188.1–297.3	188.1–297.3	187.8–292.2	187.8–292.2	189.3–306.5	189.3–306.5
T_{sat} (°C)	76.5–93.1	76.5–93.1	76.4–92.5	76.4–92.5	76.7–94.3	76.7–94.3
T_{in} (°C)	60.5–83.2	60.5–81.0	60.2–83.3	60.2–81.8	60.8–84.1	60.8–84.1
$x_{e,in}$	−0.29 to −0.09	−0.29 to −0.09	−0.28 to −0.10	−0.28 to −0.11	−0.29 to −0.09	−0.29 to −0.09
P_R	0.09–0.16	0.10–0.16	0.10–0.16	0.10–0.16	0.09–0.17	0.10–0.17
Data points	97	65	80	65	97	86

two half sidewalls, and applying the fin analysis method. The method used here uses experimentally determined effective heat flux, q''_{eff}, and difference between the local micro-channel bottom wall temperature, $T_{w,b}$, and local bulk fluid temperature, T_f.

$$h = \frac{q''_{eff}(W_{ch} + W_w)}{(T_{w,b} - T_f)(W_{ch} + 2\eta H_{ch})}, \tag{1}$$

where q''_{eff}, η, and m are the effective heat flux, fin efficiency and fin parameter, which are defined, respectively, as $q''_{eff} = k_s(T_b - T_t)/H_b$, $\eta = tanh(mH_{ch})/mH_{ch}$, and $m = \sqrt{2h/k_s W_W}$. In these relations, T_b and T_t are bottom and top temperatures measured by pairs of thermocouples inserted in the copper block beneath the micro-channel at five axial locations. As discussed in [25], the micro-channel bottom wall temperature, $T_{b,w}$, and the bulk fluid temperature, T_f, are given by $T_{w,b} = T_t - q''_{eff} H_t/k_s$ and $T_{f,n+1} = T_{f,n} + q''_{eff}(W_{ch} + W_W)\Delta z/(\dot{m} c_{p,f})$ for $x_e < 0$, $T_f = T_{sat}$ for $0 \leqslant x_e \leqslant 1$, and $T_{f,n+1} = T_{f,n} + q''_{eff}(W_{ch} + W_W)\Delta z/(\dot{m} c_{p,g})$ for $1 < x_e$, where the saturation temperature, T_{sat}, is determined from the local saturation pressure. The thermodynamic equilibrium quality along the channel is determined according to

$$x_e = -\frac{c_{p,f}(T_{sat} - T_f)}{h_{fg}} \quad \text{for } x_e < 0, \tag{2a}$$

$$x_{e,n+1} = x_{e,n} + \frac{q''_{eff}(W_{ch} + W_W)\Delta z}{\dot{m} h_{fg}} \quad \text{for } 0 \leqslant x_e \leqslant 1, \tag{2b}$$

and

$$x_e = 1 + \frac{c_{p,g}(T_f - T_{sat})}{h_{fg}} \quad \text{for } 1 < x_e. \tag{2c}$$

2.2. Assessment of correlations

The experimentally determined local two-phase heat transfer coefficient, h_{tp}, is identified for the spatial span where $x_e > 0$ and compared to predictions of several popular correlations. As shown in Table 2, there correlations are categorized into three different types: (1) those based on either a nucleate boiling (*nb*) relation or convective boiling (*cb*) relation [26–33], (2) those based on the maximum of value determined from *nb* and *cb* relations [34–36], and (3) correlations based on superpositioning of *nb* and *cb* relations [37,39–42]. It should be emphasized that, excepting the correlation of Kim and Mudawar [42], all other correlations were developed for circular channels with uniform circumferential heating, or rectangular channels with uniform four-sided heating. When assessing the predictive accuracy of these correlations against the present data for rectangular channels with three-sided heating, the relation $h_{tp} = h_{tp,cir}(Nu_3/Nu_4)$ is used [42], where $h_{tp,cir}$ is the value predicted from the original correlation, and Nu_3 and Nu_4 are the single-phase Nusselt numbers for laminar flow with three-sided and four-sided heating, respectively.

$$Nu_3 = 8.235(1 - 1.883\beta + 3.767\beta^2 - 5.814\beta^3 + 5.361\beta^4 - 2.0\beta^5) \tag{3a}$$

and

$$Nu_3 = 8.235(1 - 1.883\beta + 3.767\beta^2 - 5.814\beta^3 + 5.361\beta^4 - 2.0\beta^5). \tag{3b}$$

Table 2 shows several of the h_{tp} correlations employ a relation for the single-phase heat transfer relation, h_{sp}, which is determined from $h_{sp} = Nu(k_f/D_h)$, where, for three-sided and four-sided heating, respectively,

$$Nu = Nu_3 \quad \text{or} \quad Nu = Nu_4 \quad \text{for } Re_f < 2000 \tag{4a}$$

and

$$Nu = 0.023\, Re_f^{0.8}\, Pr_f^{0.4} \quad \text{for } Re_f > 2000 \tag{4b}$$

The multiplier Nu_3/Nu_4 is not applied to the correlation of Kim and Mudawar [42], which accounts for partial or full circumferential heating by the ratio of heated perimeter to wetted perimeter, P_H/P_F.

Figs. 1–3 compare the experimentally determined local two-phase heat transfer coefficient corresponding to $x_e > 0$ at five different axial locations where the copper block temperatures are measured. The predictive accuracy of a correlation is determined by mean absolute error, which is defined as

$$\text{MAE} = \frac{1}{N}\sum\left|\frac{h_{tp,pred} - h_{tp,exp}}{h_{tp,exp}}\right| \times 100\%. \tag{5}$$

Two additional parameters, θ and ξ, indicate the percentages of data points predicted within ±30% and ±50%, respectively. Subscripts $T1$ to $T5$ indicate the five axial locations, z = 12.7, 44.5, 76.2, 108.0 and 137.7 mm, where the copper block temperatures are measured. The open symbols represent two-phase heat transfer coefficient data measured during tests incurring *severe pressure drop oscillation* [25]; these data points are excluded from calculations of MAE, θ and ξ since the correlations are not intended for unstable conditions.

Fig. 1 compares the experimentally-determined local two-phase heat transfer coefficient, h_{tp}, at the five different axial locations with predictions of the first group of correlations in Table 2 that are based on a nucleate boiling (*nb*) or convective boiling (*cb*) relation. Separate comparisons are shown for the horizontal flow, vertical upflow and vertical downflow data. Notice that the data designated by open symbols, which correspond to severe pressure drop oscillation and are excluded from calculations of MAE, θ and ξ, show large deviations from both the other data and predictions. Overall, the correlations in this group give poor

Table 2
Saturated boiling heat transfer correlations.

Author(s)	Correlation	Remarks
Correlations based on either a nucleate boiling (*nb*) relation or convective boiling (*cb*) relation		
Lazarek and Black [26]	$h_{tp} = 30\,Re_{fo}^{0.857}\,Bo^{0.714}\,\frac{k_f}{D_h}$, $Re_{fo} = \frac{GD_h}{\mu_f}$, $Bo = \frac{q''_H}{Gh_{fg}}$	*nb*-Based, single circular copper tubes, D_h = 3.15 mm, R133, vertical upflow and downflow, G = 125–750 kg/m^2 s, q''_H =0–40 W/cm^2, x_e = 0–0.8
Cooper [27]	$h_{tp} = 55\,P_R^{0.12}(-\log_{10}P_R)^{-0.55}M^{-0.5}q''^{0.67}_H$	*nb*-Based, pool boiling, stainless steel, copper, platinum, nickel, aluminum, brass, circular, rectangular, wire, hydrogen, deuterium, helium, methane, water, neon, nitrogen, ethane, methanol, oxygen, propane, ethanol, n-butane, benzene, R11, R12, R13, R113, R114, R115, R21, R22, R13B1, R226, RC318, SF6, >6000 data points from over100 sources
Tran et al. [28]	$h_{tp} = 8.4\times10^5(Bo^2We_{fo})^{0.3}\left(\frac{\rho_g}{\rho_f}\right)^{0.4}$, $We_{fo} = \frac{G^2D_h}{\rho_f\sigma}$	*nb*-Based, single circular/rectangular tubes, D_h = 2.4 mm for rectangular, 2.46, 2.92 mm for circular, R12, R113, horizontal, G = 44–832 kg/m^2 s, q''_H =0.36–12.9 W/cm^2, x_e = 0.2–0.94, 249 data points
Lee and Lee [29]	$h_{tp} = E\,h_{sp}$ $h_{sp} = 0.023\,Re_{fo}^{0.8}\,Pr_f^{0.4}\,\frac{k_f}{D_h}$, $E = 10.3\beta^{0.398}\phi_f^{0.598}$ $\phi_f = \left(1+\frac{C}{X}+\frac{1}{X^2}\right)^{0.5}$, $C = 6.185\times10^{-2}Re_{fo}^{0.726}$, $Re_{fo} = \frac{GD_h}{\mu_f}$	*cb*-Based, single rectangular, D_h = 0.784–3.636 mm, R113, horizontal, stainless steel, G = 50–200 kg/m^2 s, q''_H =1.5 W/cm^2, x_e = 0.15–0.75
Warrier et al. [30]	$h_{tp} = E\,h_{sp}$ $E = 1.0 + 6.0Bo^{1/16} - 5.3(1-855\,Bo)x_e^{0.65}$, $h_{tp} = 0.023\,Re_{fo}^{0.8}\,\mathrm{Pr}_f^{0.4}\,\frac{k_f}{D_h}$	*nb*-Based, multi (N = 5) rectangular aluminum, D_h = 0.75 mm, FC84, horizontal, G = 557–1600 kg/m^2 s, q''_H =0–5.99 W/cm^2, x_e = 0–0.5
Agostini and Bontemps [31]	for $x_e \leqslant 0.43$, $h_{tp} = 28\,q''^{2/3}_H G^{-0.26}x_e^{-0.10}$ for $x_e > 0.43$, $h_{tp} = 28\,q''^{2/3}_H G^{-0.64}x_e^{-2.08}$	*nb*-Based, multi (N = 11) rectangular aluminum, D_h = 2.01 mm, R134a, vertical upflow, G = 90–295 kg/m^2 s, q''_H =0.6–3.16 W/cm^2, x_e = 0.26–1
Li and Wu [32]	$h_{tp} = 334\,Bo^{0.3}\left(BdRe_f^{0.36}\right)^{0.4}\left(\frac{k_f}{D_h}\right)$, $Bd = \frac{g(\rho_f-\rho_g)D_h^2}{\sigma}$	*nb*-Based, single/multi circular/rectangular, D_h = 0.16–3.01 mm, R11, R12, R123, R134a, R141b, R22, R236fa, R245fa, FC77, FC84, water, CO_2, propane, horizontal, vertical upflow, G = 23.4–3570.0 kg/m^2 s, q''_H =0–115.0 W/cm^2, x_e = 0–1, 3744 data points from 26 sources
Oh and Son [33]	$h_{tp} = 0.034\,Re_f^{0.8}\,Pr_f^{0.3}\left[1.58\left(\frac{1}{X_{tt}}\right)^{0.87}\right]\left(\frac{k_f}{D_h}\right)$	*cb*-Based, single circular copper, D_h = 1.77, 3.36, 5.35 mm, R134a, R22, horizontal
Correlations based on maximum of values determined from nucleate boiling (*nb*) and convective boiling (*cb*) relations		
Shah [34,35]	$h_{tp} = Max(E,S)h_{sp}$ $S = 1.8/N^{0.8}$, $h_{sp} = 0.023\,Re_f^{0.8}\,Pr_f^{0.4}\,\frac{k_f}{D_h}$ for $N > 1.0$, $E = 1 + 46Bo^{0.5}$ for $Bo < 3\times10^{-5}$ $E = 230Bo^{0.5}$ for $Bo > 3\times10^{-5}$ for $0.1 < N \leqslant 1.0$, $E = FBo^{0.5}\exp(2.74N^{-0.1})$ for $N \leqslant 0.1$, $E = F\,Bo^{0.5}\exp(2.47N^{-0.15})$ F = 14.7 for $Bo \geqslant 11\times10^{-4}$ or F = 15.43 for $Bo < 11\times10^{-4}$ $N = Co$ for vertical tube, $N = Co$ for horizontal tube with $Fr_f \geqslant 0.04$ $N = 0.38Fr_f^{-0.3}Co$ for horizontal tube with $Fr_f < 0.04$ $Re_f = \frac{G(1-x)D_h}{\mu_f}$, $Co = \left(\frac{1-x}{x}\right)^{0.8}\left(\frac{\rho_g}{\rho_f}\right)^{0.5}$, $Fr_f = \frac{G^2}{\rho_f^2 gD_h}$	Single, circular, R11, R113, R12, R22, water, cyclohexane, horizontal, vertical upflow/downflow, 780 data points from 19 sources
Ducoulomnier et al. [36]	$h_{tp} = Max(h_{nb}, h_{cb})$ $h_{nb} = 131\,P_R^{-0.0063}(-\log_{10}P_R)^{-0.55}M^{-0.5}q''^{0.58}_H$, for $Bo > 1.1\times10^{-4}$, $h_{cb} = \left[1.47\times10^4\,Bo + 0.93\left(\frac{1}{X_{tt}}\right)^{2/3}\right]h_{sp,fo}$ for $Bo < 1.1\times10^{-4}$, $h_{cb} = \left[1 + 1.80\left(\frac{1}{X_{tt}}\right)^{0.986}\right]h_{sp}$ $h_{sp} = 0.023Re_{fo}^{0.8}Pr_f^{0.4}\,\frac{k_f}{D_h}$	Single, circular stainless steel, D_h = 0.529 mm, CO_2, horizontal, G = 200–1200 kg/m^2 s, q''_H =1–3 W/cm^2, 2710 data points
Correlations based on superpositioning of nucleate boiling (*nb*) and convective boiling (*cb*) relations		
Chen [37]	$h_{tp} = Eh_{sp} + Sh_{nb}$ $h_{nb} = 0.00122\left(\frac{k_f^{0.79}c_{pf}^{0.45}\upsilon_g^{0.24}}{\sigma^{0.5}\mu_f^{0.29}h_{fg}^{0.24}\upsilon_f^{0.49}}\right)\Delta T_{sat}^{0.24}\Delta P_{sat}^{0.75}$ $E = (1+\frac{1}{X^{0.5}})^{1.78}$, $S = 0.9622 - 0.5822\tan^{-1}\left(\frac{Re_f E^{1.25}}{6.18\times10^4}\right)$ E, S from Edelstein et al. [38]	Water, methanol, cyclohexan, pentane, heptane, benzene, vertical upflow/downflow, over 600 data points from 10 sources
Gungor and Winterton [39]	$h_{tp} = Eh_{sp} + Sh_{nb}$, $h_{sp} = 0.023\,Re_{fo}^{0.8}\,Pr_f^{0.4}\,\frac{k_f}{D_h}$ $E = 1 + 24000\,Bo^{1.16} + 1.37\left(\frac{1}{X_{tt}}\right)^{0.86}$, $S = \left(1 + 1.15\times10^{-6}E^2\,Re_f^{1.17}\right)^{-1}$ $h_{nb} = h_{tp,Cooper}$	Circular, D_h = 2.95–32 mm, R11, R113, R114, R12, R22, water, ethylene glycol, horizontal, vertical upflow/downflow, G = 12.4–8179.3 kg/m^2 s, q''_H =0.03–262 W/cm^2, 4300 data points from 28 sources
Liu and Winterton [40]	$h_{tp} = [(Eh_{sp})^2 + (Sh_{nb})^2]^{0.5}$, $h_{sp} = 0.023\,Re_{fo}^{0.8}\,Pr_f^{0.4}\,\frac{k_f}{D_h}$ for horizontal tube with $Fr_f \leqslant 0.05$	Same data as Gungor and Winterton [39]

Table 2 (*continued*)

Author(s)	Correlation	Remarks
	$E = \left[Fr_f^{(0.1-2Fr_f)}\right]\left[1 + x_e Pr_f\left(\frac{\rho_f}{\rho_g} - 1\right)\right]^{0.35}$, $S = (Fr_f^{0.5})\left(1 + 0.055E^{0.1}\,Re_{fo}^{0.16}\right)^{-1}$ for vertical tube and horizontal tube with $Fr_f > 0.05$ $E = \left[1 + x_e\,Pr_f\left(\frac{\rho_f}{\rho_g} - 1\right)\right]^{0.35}$, $S = \left(1 + 0.055E^{0.1}Re_{fo}^{0.16}\right)^{-1}$ $h_{nb} = h_{tp,Cooper}$	
Bertsch et al. [41]	$h_{tp} = Eh_{cb} + Sh_{nb}$ $h_{cb} = h_{sp,fo}(1 - x_e) + h_{sp,go}x_e$ $E = 1 + 80(x_e^2 - x_e^6)\exp(-0.6N_{conf})$, $S = 1 - x_e$ $h_{sp,fo} = \left(3.66 + \frac{0.668\frac{D_h}{L}Re_{fo}Pr_f}{1+0.04\left[\frac{D_h}{L}Re_{fo}Pr_f\right]^{2/3}}\right)\frac{k_f}{D_h}$, $h_{sp,go} = \left(3.66 + \frac{0.668\frac{D_h}{L}Re_{go}Pr_g}{1+0.04\left[\frac{D_h}{L}Re_{go}Pr_g\right]^{2/3}}\right)\frac{k_g}{D_h}$ $N_{conf} = \sqrt{\frac{\sigma}{g(\rho_f-\rho_g)D_h^2}}$, $Re_{fo} = \frac{GD_h}{\mu_f}$, $Re_{go} = \frac{GD_h}{\mu_g}$	Circular/rectangular, D_h = 2.95–32 mm, R11, R113, R114, R12, R22, water, ethylene glycol, horizontal, vertical upflow/downflow, G = 20–3000 kg/m^2 s, q''_H =0.4–115 W/cm^2, x_e = 0–1, 3899 data points from 14 sources
Kim and Mudawar [42]	$h_{tp} = \left(h_{nb}^2 + h_{cb}^2\right)^{0.5}$ $h_{nb} = \left[2345\left(Bo\frac{P_H}{P_F}\right)^{0.70}P_R^{0.38}(1 - x_e)^{-0.51}\right]\left(0.023\,Re_f^{0.8}Pr_f^{0.4}\,\frac{k_f}{D_h}\right)$ $h_{cb} = \left[5.2\left(Bo\frac{P_H}{P_F}\right)^{0.08}We_{fo}^{-0.54} + 3.5\left(\frac{1}{X_{tt}}\right)^{0.94}\left(\frac{v_f}{v_g}\right)^{0.25}\right]\left(0.023\,Re_f^{0.8}Pr_f^{0.4}\,\frac{k_f}{D_h}\right)$ $Bo = \frac{q''_H}{Gh_{fg}}$, $P_R = \frac{P}{P_{crit}}$, $Re_f = \frac{G(1-x_e)D_h}{\mu_f}$, $We_{fo} = \frac{G^2D_h}{\rho_f\sigma}$, $X_{tt} = \left(\frac{\mu_f}{\mu_g}\right)^{0.1}\left(\frac{1-x_e}{x_e}\right)^{0.9}\left(\frac{\rho_g}{\rho_f}\right)^{0.5}$	Circular/rectangular, D_h = 0.19–6.5 mm, FC72, R11, R113, R123, R1234yf, R1234ze, R134a, R152a, R22, R236fa, R245fa, R32, R404A, R407C, R410A, R417A, CO_2, water, horizontal, vertical upflow/downflow, G = 19–1608 kg/m^2 s, x_e = 0–1, 12,974 data points from 31 sources

predictions of the closed symbols, corresponding to tests free from severe pressure drop oscillation, with those of Lazarek and Black [26], Fig. 1(a), Cooper [27], Fig. 1(b), Tran et al. [28], Fig. 1(c), Lee and Lee [29], Fig. 1(d), and Warrier et al. [30], Fig. 1(e), underpredicting the present data. The correlations by Oh and Son [33], Fig. 1(g), and of Li and Wu [32], Fig. 1(h), show weak trends, evidenced by large MAE values. Only the correlation by Agostini and Bontemps [31], Fig. 1(f), which was developed from vertical upflow multi-channel data gives relatively good predictions, with MAE = 17.2%, 16.1%, and 13.4%, for the present horizontal flow, vertical upflow, and vertical downflow data, respectively.

Fig. 2 compares the experimentally determined local two-phase heat transfer coefficient with predictions of the second group of correlations, where the heat transfer coefficient is based on the maximum value from nucleate boiling (*nb*) and convective boiling (*cb*) relations. Both correlations yield fair accuracy, albeit with significant scatter, with that of Shah [34,35], Fig. 2(a), yielding MAEs of 27.8%, 26.8% and 24.1% for horizontal flow, vertical upflow and vertical downflow, respectively, and corresponding MAEs of the correlation by Ducoulomnier et al. [36], Fig. 2(b), of 25.7%, 24.8% and 21.7%.

Fig. 3 compares the experimentally determined local two-phase heat transfer coefficient with predictions of the third group of correlations, which involve superpositioning of nucleate boiling (*nb*) and convective boiling (*cb*) relations. The correlations in this group show relatively good predictions for the different orientations, with the recent correlation by Kim and Mudawar [42], Fig. 3(e), yielding the best predictions, with MAEs of 19.0%, 19.9% and 16.9% for horizontal flow, vertical upflow and vertical downflow, respectively. The superior accuracy of this correlation can be traced to its reliance on the largest consolidated database consisting of 10,805 mini/micro-channel data points amassed from 31 sources, including 18 working fluids, hydraulic diameters of 0.19–6.5 mm, mass velocities of 19–1608 kg/m^2 s, liquid-only Reynolds numbers of 57–49,820, qualities of 0–1, and reduced pressures of 0.005–0.69.

Figs. 4–6 compare, for six narrow ranges of mass velocity, the variations of experimentally determined local heat transfer coefficient with quality for horizontal flow, vertical upflow and vertical downflow with the predictions of different correlations. Fig. 4 compares data with the first group of correlations based on *nb* or *cb* relations. Fig. 5 shows comparisons with the second group of correlations based on the maximum of values determined from *nb* and *cb* relations. Fig. 6 compares data with the third group of correlations based on superpositioning of *nb* and convective boiling *cb* relations. Excepting the highest mass velocity range of G = 607.6–644.5 kg/m^2 s, the data show increasing x_e causes an initial upstream decrease in h_{tp}, followed by an increase in h_{tp} downstream. However, Figs. 4 and 5 show that most correlations from the first two groups of correlations fail to capture the trend of decreasing h_{tp} for low x_e. Correlations from the first group that do capture this trend are those of Warrier et al. [30] and Agostini and Bontemps [31], the latter being the one that proved most accurate in the prediction of h_{tp} as shown in Fig. 1(f). Fig. 5 shows that the correlations by Shah [34,35] and Ducoulomnier et al. [36] also fail to capture the trend of decreasing h_{tp} for low x_e. Fig. 6 shows correlations from the third group are also unable to capture this trend. Overall, the third group of correlations shows better predictions with increasing x_e and increasing G.

3. Assessment of pressure drop correlations

3.1. Pressure drop determination

As described in part 1 of this study [25], the total pressure drop, ΔP_{tot}, is determined from the difference in pressures measured by absolute pressure transducers connected to the inlet and outlet of the test module. The total pressure drop consists of several components, including upstream contraction, ΔP_c, upstream subcooled liquid region, $\Delta P_{sp,f}$, where $x_e < 0$, saturated two-phase region, ΔP_{tp}, where $0 < x_e < 1$, superheated single-phase vapor region, $\Delta P_{sp,g}$, where $x_e > 0$, and downstream expansion, ΔP_e. It should be emphasized that not all components are encountered in a test. For example, $\Delta P_{sp,f} = 0$ when the flow enters the channels in saturated liquid state or as a two-phase mixture. Additionally, for most operating conditions, $\Delta P_{sp,g} = 0$, since tests are terminated before wall dryout or critical heat flux (CHF) are incurred.

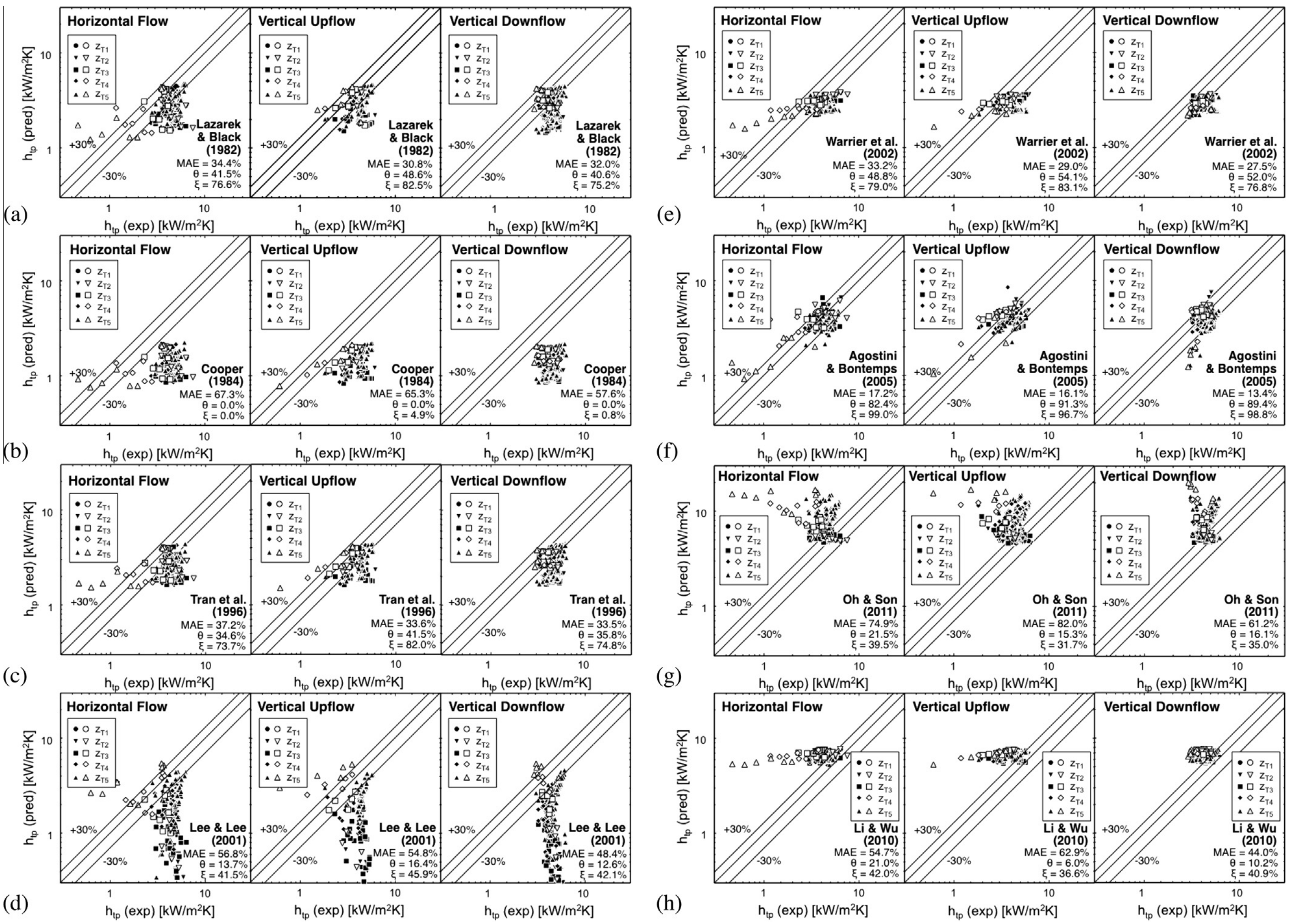

Fig. 1. Comparison of experimentally determined local heat transfer coefficient at five different axial locations for horizontal flow, vertical upflow and vertical downflow with predictions based on nucleate boiling (*nb*) or convective boiling (*cb*) correlations of (a) Lazarek and Black [26], (b) Cooper [27], (c) Tran et al. [28], (d) Lee and Lee [29], (e) Warrier et al. [30], (f) Agostini and Bontemps [31], (g) Li and Wu [32], and (h) Oh and Son [33]. Open symbols correspond to data for severe pressure oscillation, which are not included in the statistical assessment of correlations.

Depending on operating conditions, pressure drop for the upstream subcooled region where $x_e < 0$ can be further divided into three sub-regions: single-phase liquid developing region, $\Delta P_{sp,d}$, single-phase liquid fully-developed region, $\Delta P_{sp,fd}$, and subcooled boiling region, ΔP_{sc}. Pressure drop in the saturated region, ΔP_{tp}, is comprised of three components: accelerational, $\Delta P_{tp,A}$, gravitational, $\Delta P_{tp,G}$, and frictional, $\Delta P_{tp,F}$.

For the conditions of the present study, the single-phase liquid developing and subcooled portions of the subcooled region account for only a small fraction of the total length of the micro-channel. Therefore, $\Delta P_{sp,d}$ and ΔP_{sc} are combined into $\Delta P_{sp,f}$, and total pressure drop is represented by

$$\Delta P_{tot} = \Delta P_c + \Delta P_{sp,f} + (\Delta_{tp,A} + \Delta P_{tp,G} + \Delta P_{sp,g} + \Delta P_{tp,F}) + \Delta P_{sp,g} + \Delta P_e. \quad (6)$$

Part 1 of the present study included relations used to calculate ΔP_c, $\Delta P_{sp,f}$, $\Delta P_{sp,g}$, ΔP_e, $\Delta P_{tp,A}$ and $\Delta P_{tp,G}$, which are also included in Table 3. Discussed below are details of the two-phase frictional pressure drop component, $\Delta P_{tp,F}$, which accounts for the largest fraction of ΔP_{tot}.

3.2. Two-phase pressure drop models

Two general approaches are used to determine pressure drop for the saturated two-phase flow region: *Homogeneous Equilibrium Model* (*HEM*) and *Separated Flow Model* (*SFM*). Following is a brief discussion of these models and associated assumptions.

3.2.1. Pressure drop data comparison with predictions Homogeneous Equilibrium Model (HEM)

By employing a variety of averaging techniques to evaluate mixture properties, *HEM* treats a two-phase mixture as a pseudo fluid that obeys standard conservation relations similar to those employed with single-phase flow. Based on the assumptions of negligible kinetic and potential energy changes and negligible flashing and compressibility, the two-phase pressure gradient for a channel with a constant flow area can be expressed as the sum of frictional, accelerational and gravitational components.

$$-\left(\frac{dP}{dz}\right)_{tp} = \frac{2}{D_h} f_{tp} G^2 v_f \left(1 + x_e \frac{v_{fg}}{v_f}\right) + G^2 v_{fg} \frac{dx_e}{dz} + \frac{g \sin\theta}{v_f + x_e v_{fg}}, \quad (7)$$

The two-phase friction factor, f_{tp}, in Eq. (7) is obtained from [42,43]

$$f_{tp} Re_{tp} = 24\left[1 - 1.3553\beta + 1.9467\beta^2 - 1.7012\beta^3 + 0.9564\beta^4 - 0.2537\beta^5\right] \quad \text{for } Re_{tp} < 2000 \quad (8a)$$

$$f_{tp} = 0.079 Re_{tp}^{-0.25} \quad \text{for } 2000 < Re_{tp} < 20{,}000, \quad (8b)$$

$$f_{tp} = 0.046 Re_{tp}^{-0.2} \quad \text{for } 20{,}000 < Re_{tp}, \quad (8c)$$

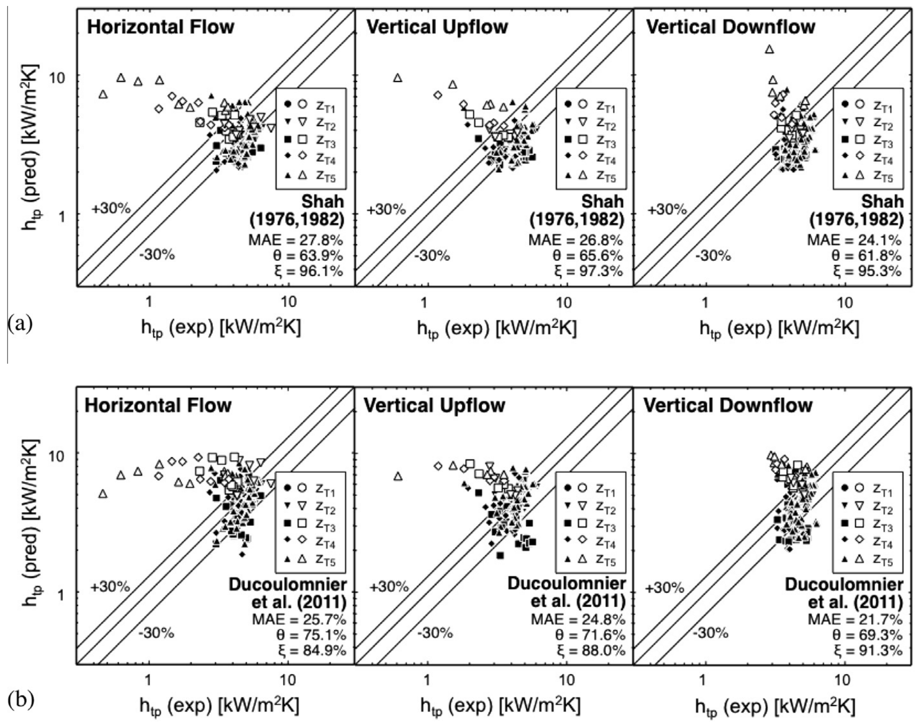

Fig. 2. Comparison of experimentally determined local heat transfer coefficient at five different axial locations for horizontal flow, vertical upflow and vertical downflow with predictions based on maximum of value from relations for nucleate boiling (*nb*) and convective boiling (*cb*) according to (a) Shah [34,35] and (b) Ducoulomnier et al. [36]. Open symbols correspond to data for severe pressure oscillation, which are not included in the statistical assessment of correlations.

where $Re_{tp} = GD_h/\mu_{tp}$, based on mixture viscosity μ_{tp}. Table 4 provides a summary of two-phase viscosity relations evaluated in the present study. When calculating the two-phase frictional pressure gradient in order to determine ΔP_{tp}, Eq. (7) is integrated between $z = 0$ and L.

Fig. 7(a)–(g) show comparisons of the experimental data with predictions of the *HEM* using the seven mixture viscosity relations from Table 4. The predictive accuracy is determined by mean absolute error, which is defined as

$$MAE = \frac{1}{N}\sum\left|\frac{\Delta P_{tot,pred} - \Delta P_{tot,\exp}}{\Delta P_{tot,\exp}}\right| \times 100\%, \tag{9}$$

as well as θ and ξ, which are defined as the percentages of data points predicted within ±30% and ±50%, respectively. Predictions using the viscosity relations of McAdams et al. [46], Akers et al. [47], Dukler et al. [50] and Lin et al. [52] show fairly good agreement with the experimental data, while those using the relations of Cicchiti et al. [48], Owens [49] and Beattie and Whalley [51] highly overpredict the data especially for low mass velocities, but show improved accuracy at high mass velocities. Of all seven viscosity relations used in conjunction with the *HEM*, the relation by Lin et al. shows the best accuracy, with MAEs of 22.0%, 28.9% and 22.8% for horizontal flow, vertical upflow and vertical downflow, respectively.

3.2.2. Pressure drop data comparison with predictions of Separate Flow Model (SFM)

Unlike the *HEM*, *SFMs* allow for differences between liquid and vapor velocities, with each phase occupying a separate portion of the flow area. Based on the *SFM*, the total pressure gradient for steady flow in a channel with a constant flow area is given by [53]

$$-\left(\frac{dP}{dz}\right)_{tp} = -\left(\frac{dP}{dz}\right)_{tp,F} - \left(\frac{dP}{dz}\right)_{tp,A} - \left(\frac{dP}{dz}\right)_{tp,G}, \tag{10}$$

where

$$-\left(\frac{dP}{dz}\right)_{tp,A} = G^2\frac{d}{dz}\left[\frac{x_e^2 v_g}{\alpha} + \frac{(1-x_e)^2 v_f}{1-\alpha}\right] \tag{11a}$$

and

$$-\left(\frac{dP}{dz}\right)_{tp,G} = [\alpha\rho_g + (1-\alpha)\rho_f]g\sin\theta. \tag{11b}$$

The void fraction, α, in the accelerational and gravitational terms can be determined using Zivi's correlation [45],

$$\alpha = \left[1 + \left(\frac{1-x_e}{x_e}\right)\left(\frac{\rho_g}{\rho_f}\right)^{2/3}\right]^{-1}. \tag{12}$$

The total pressure gradient, ΔP_{tp}, is obtained by integrating Eq. (10) between $z = 0$ and L using an appropriate correlation for the frictional pressure gradient.

Table 5 summarizes popular correlations for the two-phase frictional pressure gradient based on the *SFM*. The first eleven correlations [54–64] were not specifically developed, but have been widely used for micro-channel applications, while the last seven correlations [53,65–70] were developed from mini/micro-channels experimental data. Comparisons between the experimental data and predictions of these correlations are provided in Figs. 8–10. The predictions using the first eleven correlations are shown in Figs. 8 and 9. The correlations by Lockhart and Martinelli [54], Friedel [55], Müller-Steinhagen and Heck [56], Mishima and Hibiki [58], Yang and Webb [59], Wang et al. [60], and Yan and Lin [61] show fair predictions of the data, with MAEs in the range of 28.7–39.5%, 22.3–42.3%, and 31.5–40.0% for horizontal flow, vertical upflow and vertical downflow, respectively. On the other hand, the correlations by Jung and Radermacher [57], Tran et al. [62], Chen et al. [63] and Yu et al. [64] yield far less favorable predictions. Notice that these correlations show no obvious superior accuracy relative to flow orientation.

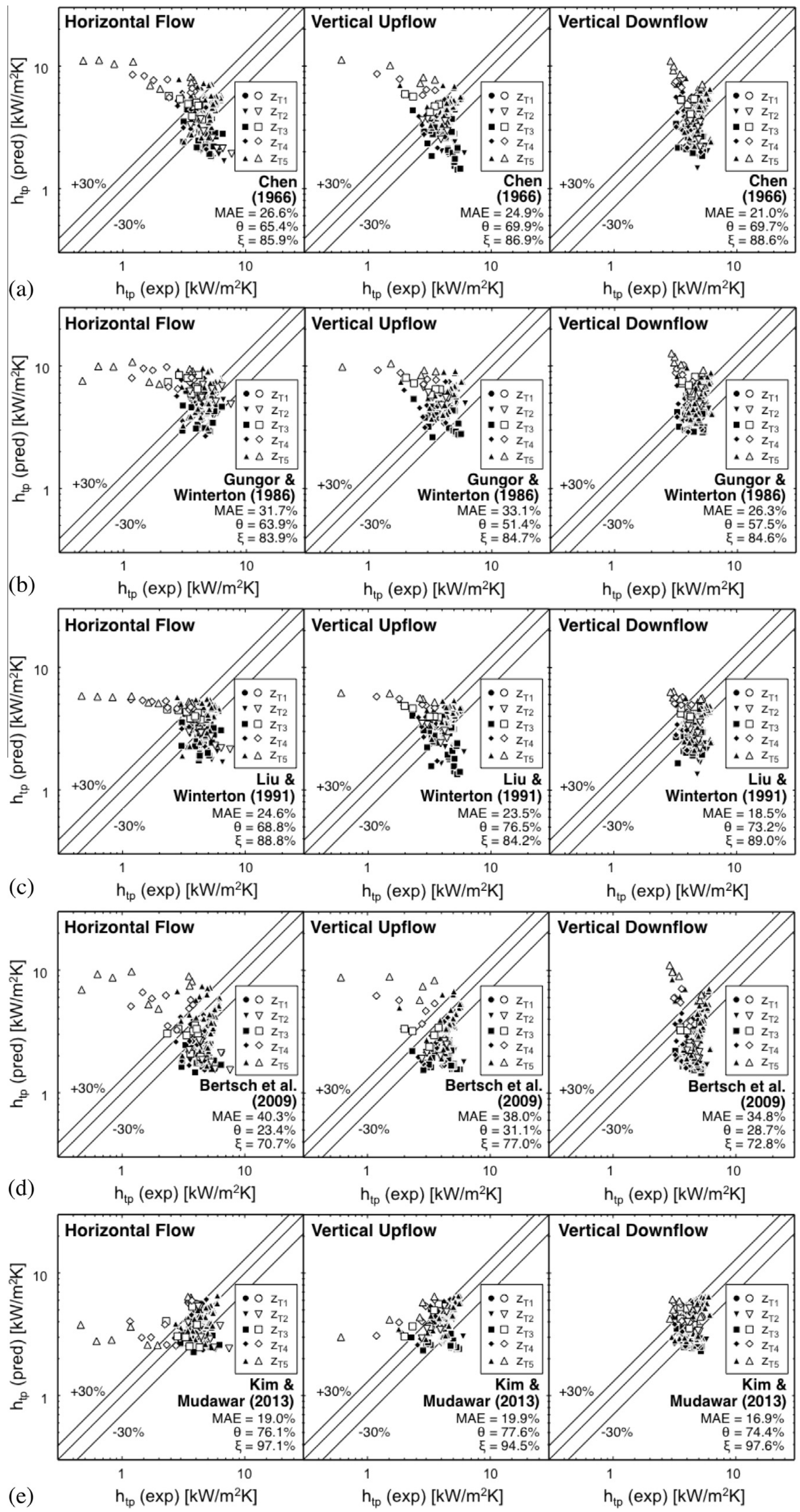

Fig. 3. Comparison of experimentally determined local heat transfer coefficient at five different axial locations for horizontal flow, vertical upflow and vertical downflow with predictions of correlations based on superpositioning of nucleate boiling (*nb*) and convective boiling (*cb*) relations by (a) Chen [37], (b) Gungor and Winterton [39], (c) Liu and Winterton [40], (d) Bertsch et al. [41], and (e) Kim and Mudawar [42]. Open symbols correspond to data for severe pressure oscillation, which are not included in the statistical assessment of correlations.

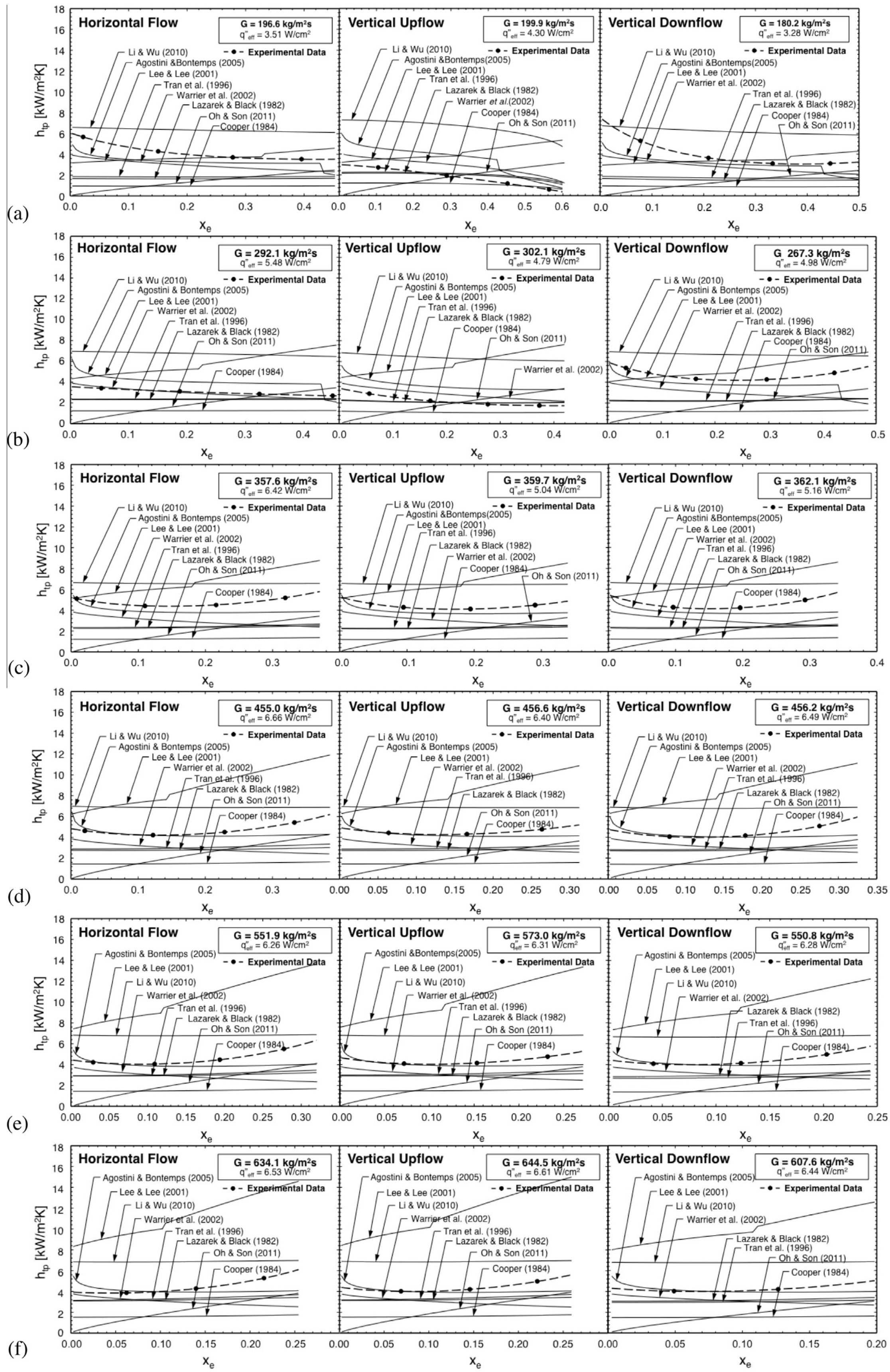

Fig. 4. Comparison of variation of experimentally determined local heat transfer coefficient with quality for horizontal flow, vertical upflow and vertical downflow with predictions of nucleate boiling (*nb*) or convective boiling (*cb*) correlations for (a) G = 180.2–199.9 kg/m^2 s, (b) G = 267.3–302.1 kg/m^2 s, (c) G = 357.6–362.1 kg/m^2 s, (d) G = 455.0–456.6 kg/m^2 s, (e) G = 550.8–573.0 kg/m^2 s, and (f) G = 607.6–644.5 kg/m^2 s.

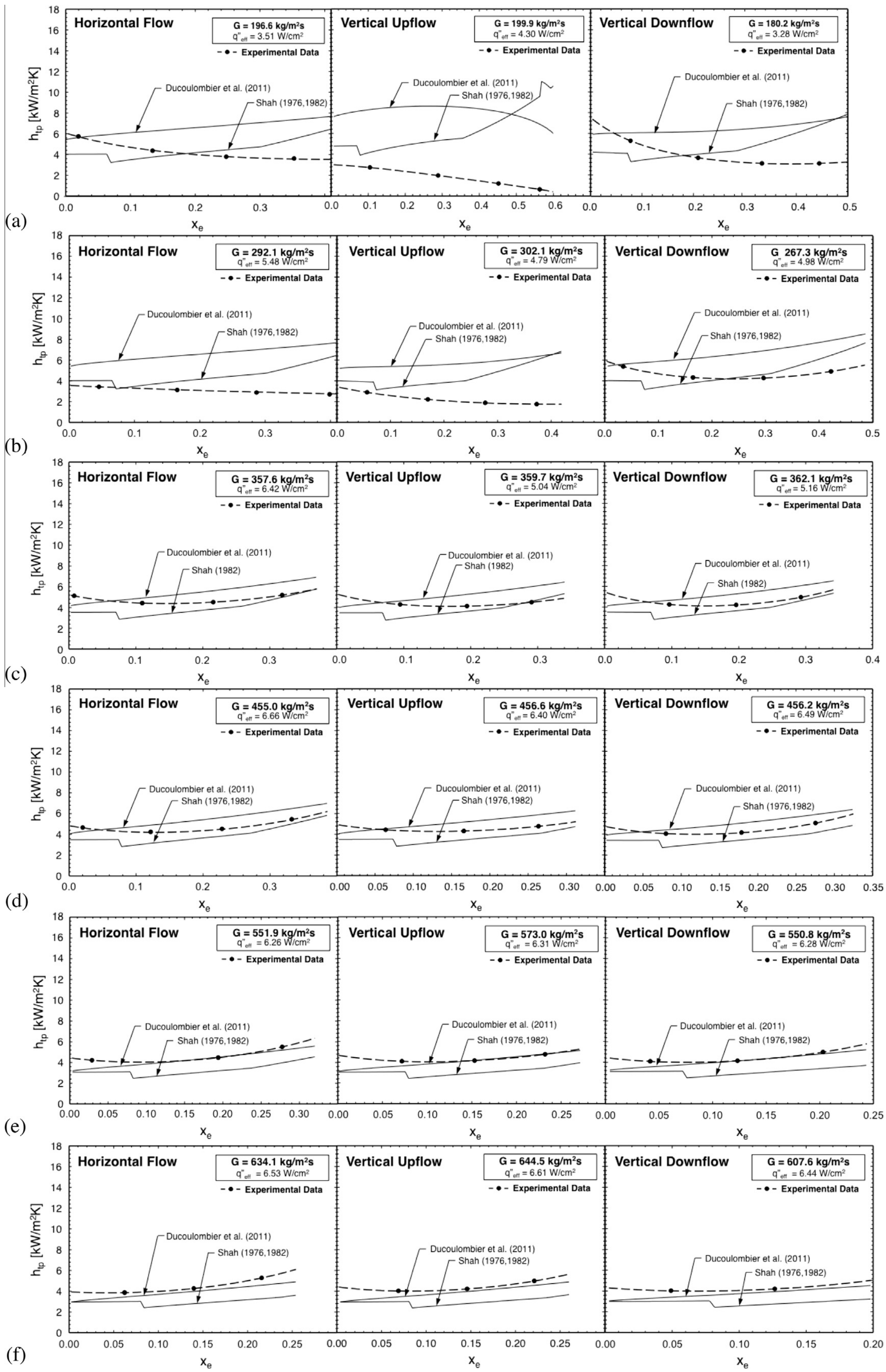

Fig. 5. Comparison of variation of experimentally determined local heat transfer coefficient with quality for horizontal flow, vertical upflow and vertical downflow with predictions of correlations based on maximum of value from relations for nucleate boiling (*nb*) and convective boiling (*cb*) for (a) G = 180.2–199.9 kg/m^2 s, (b) G = 267.3–302.1 kg/m^2 s, (c) G = 357.6–362.1 kg/m^2 s, (d) G = 455.0–456.6 kg/m^2 s, (e) G = 550.8–573.0 kg/m^2 s, and (f) G = 607.6–644.5 kg/m^2 s.

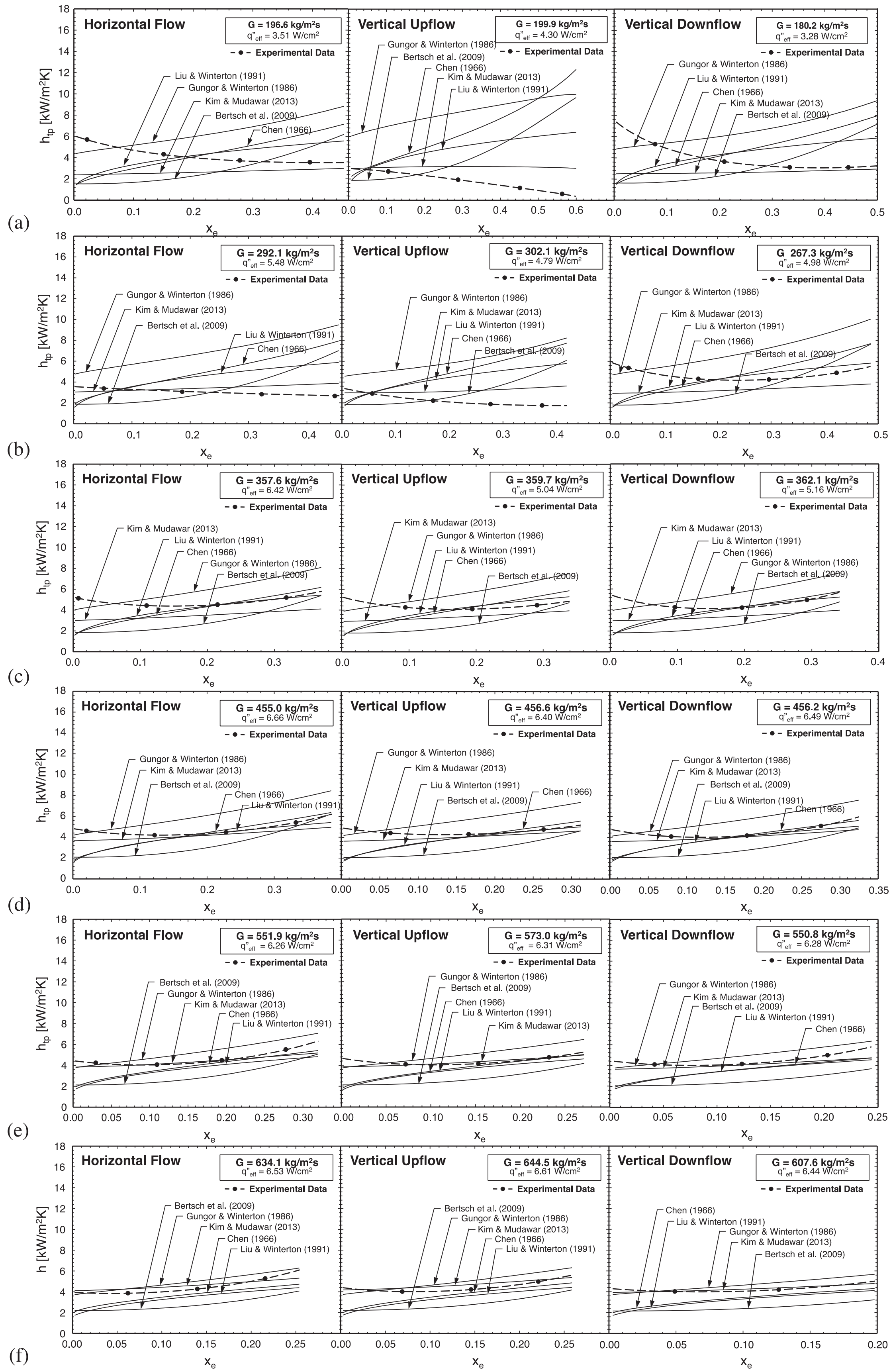

Fig. 6. Comparison of variation of experimentally determined local heat transfer coefficient with quality for horizontal flow, vertical upflow and vertical downflow with predictions of correlations based on superpositioning of nucleate boiling (*nb*) and convective boiling (*cb*) relations for (a) G = 180.2–199.9 kg/m^2 s, (b) G = 267.3–302.1 kg/m^2 s, (c) G = 357.6–362.1 kg/m^2 s, (d) G = 455.0–456.6 kg/m^2 s, (e) G = 550.8–573.0 kg/m^2 s, and (f) G = 607.6–644.5 kg/m^2 s.

Table 3
Pressure drop components [44].

	Correlation
Area changes	$\Delta P_c = \frac{G^2 v_f}{2}\left[\left(\frac{1}{C_c}-1\right)^2+(1-\sigma_c^2)\right]\left[1+\frac{v_{fg}x_{e,in}}{v_f}\right]$ $\Delta P_e = G^2\sigma_c(\sigma_c-1)v_f\left[1+\frac{v_{fg}x_{e,out}}{v_f}\right]$ $C_c = 1-\frac{1-\sigma_c}{2.08(1-\sigma_c)+0.5371}$, $\sigma_c = \frac{W_{ch}H_{ch}N_{ch}}{W_p H_p}$
Single-phase liquid and vapor regions	$\Delta P_{sp,k} = \frac{2L_{sp,k}}{D_h} f_{sp,k} G^2 v_k$ for $Re_k < 2000: f_{sp,k}Re_k = 24[1-1.3553\beta+1.9467\beta^2-1.7012\beta^3+0.9564\beta^4-0.2537\beta^5]$ for $2000 < Re_k < 20,000: f_{sp,k} = 0.079 Re_k^{-0.25}$ for $20,000 < Re_k: f_{sp,k} = 0.046 Re_k^{-0.2}$ $Re_k = \frac{GD_h}{\mu_k}$ $k = f$ for liquid, $k = g$ for vapor
Two-phase region	Accelerational: $\Delta P_{tp,A} = \int_0^{L_{tp}} -\left(\frac{dP}{dz}\right)_A dz$ $-\left(\frac{dP}{dz}\right)_A = G^2\frac{d}{dz}\left[\frac{x_e^2 v_g}{\alpha}+\frac{(1-x_e)^2 v_f}{1-\alpha}\right]$ Gravitational: $\Delta P_{tp,G} = \int_0^{L_{tp}} -\left(\frac{dP}{dz}\right)_G dz$ $-\left(\frac{dP}{dz}\right)_G = \bar{\rho} g\sin\theta = \left[\frac{\alpha}{v_g}+\frac{(1-\alpha)}{v_f}\right]g\sin\theta$ Void fraction: $\alpha = \left[1+\left(\frac{1-x_e}{x_e}\right)\left(\frac{v_f}{v_g}\right)\right]^{-1}$ when used with HEM, $\alpha = \left[1+\left(\frac{1-x_e}{x_e}\right)\left(\frac{v_f}{v_g}\right)^{2/3}\right]^{-1}$ when used with SFM [45]

Table 4
Mixture viscosity relations used in HEM.

	Viscosity relation
McAdams et al. [46]	$\frac{1}{\mu_{tp}} = \frac{x_e}{\mu_g}+\frac{1-x_e}{\mu_f}$
Akers et al. [47]	$\mu_{tp} = \frac{\mu_f}{\left[(1-x_e)+x_e\left(\frac{v_g}{v_f}\right)^{0.5}\right]}$
Cicchitti et al. [48]	$\mu_{tp} = x_e\mu_g+(1-x_e)\mu_f$
Owens [49]	$\mu_{tp} = \mu_f$
Dukler et al. [50]	$\mu_{tp} = \frac{x_e v_g \mu_g+(1-x_e)v_f\mu_f}{x_e v_g+(1-x_e)v_f}$
Beattie and Whalley [51]	$\mu_{tp} = \omega\mu_g+(1-\omega)(1+2.5\omega)\mu_f$ $\omega = \frac{x_e v_g}{v_f+x_e v_{fg}}$
Lin et al. [52]	$\mu_{tp} = \frac{\mu_f\mu_g}{\mu_g+x_e^{1.4}(\mu_f-\mu_g)}$

The predictions of the correlations developed from mini/micro-channel data are shown in Fig. 10. Overall, these correlations show better accuracy than those in Figs. 8 and 9. The correlations of Lee and Lee [65], Hwang and Kim [66] and Zhang et al. [69] slightly underpredict the data, while those of Sun and Mishima [67] and Li and Wu [68,70] overpredict. These correlations to do not appear to provide superior accuracy relative to any particular flow orientation.

Among all the correlations examined in Figs. 8–10, Kim and Mudawar's [53] shows the best predictive capability, with MAEs of 24.2%, 30.3% and 24.1% for horizontal flow, vertical upflow, and vertical downflow, respectively. The superior accuracy of this correlation can be attributed to reliance on the most recent and most comprehensive consolidated database consisting of 2378 mini/micro-channel data points from 16 sources. The database encompasses 9 working fluids, hydraulic diameters from 0.349 to 5.35 mm, mass velocities from 33 to 2738 kg/m^2 s, liquid-only Reynolds numbers from 156 to 28,010, qualities from 0 to 1, reduced pressures from 0.005 to 0.78, and both single-channel and multi-channel data.

4. Design criteria for reduced gravity space systems

4.1. Rationale

Three important criteria for implementing micro-channel flow boiling in space systems are:

(1) Avoiding the large pressure drops associated with two-phase flow boiling in micro-channels to minimize power consumption in a space vehicle's thermal control system (TCS).
(2) Avoiding critical heat flux (CHF) in the TCS evaporator.
(3) Negating the influence of body force on two-phase flow and heat transfer.

Discussed below are means to simultaneously achieve these criteria.

4.2. Avoiding high pressure drop

High pressure drop is a primary concern when implementing flow boiling in micro-channels. This concern stems from both the use of small hydraulic diameter, and appreciable vapor production within the micro-channel, especially when dissipating high heat fluxes.

In the first part of this study [25], pressure drop data were presented for flow boiling in micro-channels in three different orientations. Two-phase friction, followed by two-phase acceleration and single-phase liquid friction, were identified as dominant components of pressure drop. As shown in [25] and Eq. (8) of the present study, these three components of pressure drop are proportional to G^2. In addition, both the two-phase frictional and accelerational components increase with increasing x_e, i.e., increasing q''_{eff}. Compounding operation at high G and q''_{eff} are two-phase instabilities. Given the predictive tools presented in this study for two-phase pressure drop, the designer of a space vehicle's TCS can conduct a parametric study of evaporator design by exploring different combinations of operating conditions, overall evaporator surface area, and micro-channel shape and size to minimize pressure drop and to avoid instabilities.

4.3. Avoiding critical heat flux (CHF)

Critical heat flux (CHF) is unquestionably the most important design parameter for any two-phase system that is subjected to a prescribed heat load, and avoiding CHF requires maintaining heat flux safely below CHF. Recent studies at the Purdue University

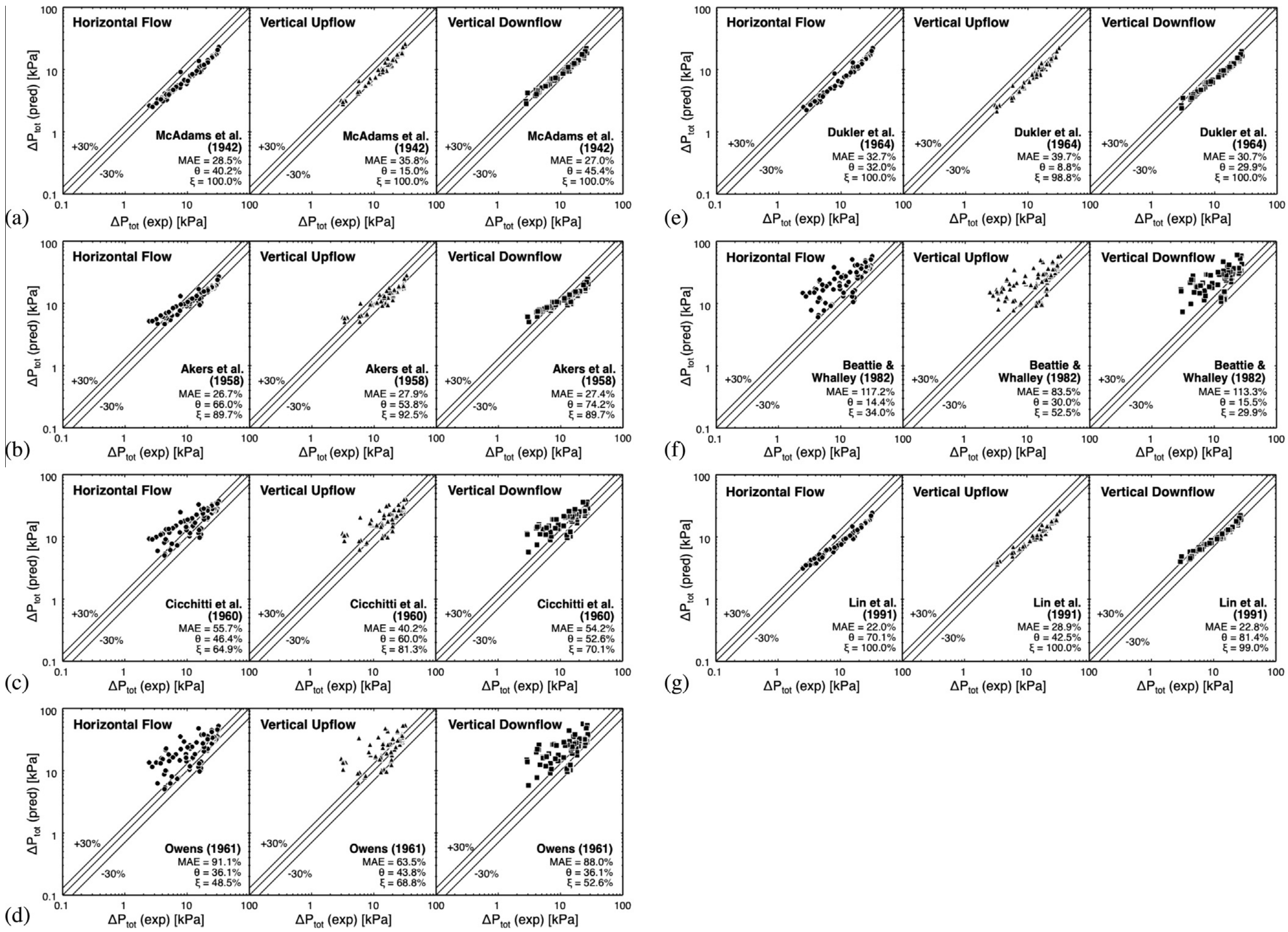

Fig. 7. Comparison of measured total pressure drop for horizontal flow, vertical upflow and vertical downflow with predictions of Homogeneous Equilibrium Model (*HEM*) using two-phase viscosity models of (a) McAdams et al. [46], (b) Akers et al. [47], (c) Cicchitti et al. [48], (d) Owens [49], (e) Dukler et al. [50], (f) Beattie and Whalley [51], and (g) Lin et al. [52].

Boiling and Two-Phase Flow Laboratory (PU-BTPFL) have yielded a detailed model for CHF in both Earth gravity [71–76] and microgravity [77,78] with both subcooled and saturated inlet conditions. Using the mechanism of interfacial lift-off as a basis for CHF, Zhang et al. [78] developed the following relation for CHF based on heated perimeter of the channel.

$$q''_m = \frac{b}{F_q}\rho_g(h_{fg} + c_{p,f}\Delta T_{sub,o})\left[\left(\frac{4\pi\sigma\delta}{\rho_g b\lambda_c^2}sin(\pi b)\right)\Bigg|_{z^*}\right]^{1/2}, \quad (13)$$

where $b = 0.2$, δ is the mean thickness of the vapor layer formed along the heated walls of the channel. In Eq. (13), F_q is the fraction of the wall heat flux that is consumed in converting near-wall liquid to vapor (remaining fraction is consumed in overcoming liquid subcooling),

$$F_q = 1 - \frac{\rho_f}{\rho_g}\frac{c_{p,f}\Delta T_{sub,o}}{h_{fg}}\left[0.00285\left(\frac{\rho_f U^2 D_h}{\sigma}\right)^{0.2}\right]. \quad (14)$$

Also in Eq. (13), λ_c is the critical wavelength of instability of the interface between a vapor layer of thickness H_g (=δ) and velocity U_g, and liquid layer of thickness H_f and velocity U_f,

$$\frac{2\pi}{\lambda_c} = \frac{\rho''_f\rho''_g(U_g - U_f)^2}{2\sigma\left(\rho''_f + \rho''_g\right)} + \sqrt{\left[\frac{\rho''_f\rho''_g(U_g - U_f)^2}{2\sigma\left(\rho''_f + \rho''_g\right)}\right]^2 + \frac{(\rho_f - \rho_g)g_n}{\sigma}}, \quad (15)$$

where $\rho''_f = \rho_f coth(2\pi H_f/\lambda_c)$ and $\rho''_g = \rho_g coth(2\pi H_g/\lambda_c)$ and g_n is the component of gravity perpendicular to heated wall. A separated flow model is used to determine the axial variations of U_f, U_g and δ along the channel. H_f for a rectangular channel with three-sided heating can be derived from $H_f = [(1-\alpha)H_{ch}W_{ch}]/[2\{(H_{ch}-\delta)+(W_{ch}-2\delta)\}]$, and q''_m from Eqs. (13) and (14) based on the values of δ and λ_c at $z^* = z_0 + \lambda_c(z^*)$, where z_0 is the location where the vapor layer velocity just exceeds the liquid layer velocity. Details of the separated flow model are provided in [75,78].

4.4. Negating influence of body force

Zhang et al. [72] derived two dimensionless parameters, Bo/We^2 and $1/Fr$, for macro-channel flows whose magnitude has to be maintained below specific values to negate body force effects perpendicular to, and parallel to the heated wall, respectively. The criteria developed by Zhang et al. are valid for subcooled inlet conditions ($x_{e,in} = 0$). More recently, Konishi et al. [76] extended these criteria to conditions involving a saturated liquid–vapor mixture at the inlet; i.e., for $x_{e,in} > 0$. Using $x_{e,in} = 0$ in the Konishi et al. criteria gives

$$\frac{Bo}{We^2} = \frac{(\rho_f - \rho_g)(\rho_f + \rho_g)^2\sigma g}{\rho_f^2\rho_g^2(G/\rho_f)^4} \leqslant 0.232 \quad (16)$$

and

$$\frac{1}{|Fr|} = \frac{(\rho_f - \rho_g)gD_h}{\rho_f(G/\rho_f)^2} \leqslant 0.02. \quad (17)$$

Table 5
Correlations for two-phase frictional pressure gradient.

Author(s)	Correlation	Remarks
	Correlations not specifically developed for mini/micro-channel flows	
Lockhart and Martinelli [54]	$\left(\frac{dP}{dz}\right)_F = \left(\frac{dP}{dz}\right)_f \phi_f^2$ $\phi_f^2 = 1 + \frac{C}{X} + \frac{1}{X^2}$, $X^2 = \left[\frac{(dP/dz)_f}{(dP/dz)_g}\right]$ $C_{vv} = 5$, $C_{tv} = 10$, $C_{vt} = 12$, $C_{tt} = 20$	Adiabatic, circular, D_h = 1.49–25.83 mm, air–water, oils, hydrocarbons, horizontal
Friedel [55]	$\left(\frac{dP}{dz}\right)_F = \left(\frac{dP}{dz}\right)_{fo} \phi_{fo}^2$ $\phi_{fo}^2 = (1-x_e)^2 + x_e^2\left(\frac{\rho_f}{\rho_g}\right)\left(\frac{f_{fo}}{f_{go}}\right) + \cdots$ $3.24 x_e^{0.78}(1-x_e)^{0.224}\left(\frac{\rho_f}{\rho_g}\right)^{0.91}\left(\frac{\mu_f}{\mu_g}\right)^{0.19}\left(1-\frac{\mu_f}{\mu_g}\right)^{0.7} Fr_H^{-0.045} We_H^{-0.035}$ $Fr_H = \frac{G^2}{g D_h \rho_H^2}$, $We_H = \frac{G^2 D_h}{\sigma \rho_H}$, $\rho_H = \frac{1}{x_e v_g + (1-x_e) v_f}$	D_h > 4 mm, R12, air–water, air–oil, horizontal, vertical upflow, 25,000 data points
Müller-Steinhagen and Heck [56]	$\left(\frac{dP}{dz}\right)_F = \left\{\left(\frac{dP}{dz}\right)_{fo} + 2\left[\left(\frac{dP}{dz}\right)_{go} - \left(\frac{dP}{dz}\right)_{fo}\right] x_e\right\}(1-x_e)^{1/3} + \left(\frac{dP}{dz}\right)_{go} x^3$	Adiabatic, D_h = 4–392 mm, R11, R12, R22, air–water, steam–water, oil, argon, hydrocarbons, neon, horizontal, vertical upflow/downflow, 9300 data points
Jung and Radermacher [57]	$\left(\frac{dP}{dz}\right)_F = \left(\frac{dP}{dz}\right)_{fo} \phi_{fo}^2$, $\phi_{fo} = 12.82 X_{tt}^{-1.47}(1-x_e)^{1.8}$ $X_{tt} = \left(\frac{\mu_f}{\mu_g}\right)^{0.1}\left(\frac{1-x_e}{x_e}\right)^{0.9}\left(\frac{\rho_g}{\rho_f}\right)^{0.5}$	Circular stainless steel, D_h = 9.1 mm, R113, R12, R22, R152a, horizontal, more than 600 data points
Mishima and Hibiki [58]	$\left(\frac{dP}{dz}\right)_F = \left(\frac{dP}{dz}\right)_f \phi_f^2$, $\phi_f^2 = 1 + \frac{C}{X} + \frac{1}{X^2}$ for rectangular channels, $C = 21[1 - \exp(-319 D_h)]$ for circular channels, $C = 21[1 - \exp(-319 D_h)]$ D_h in mm	Circular Pyrex glass, adiabatic, D_h = 1.05–4.08 mm, air–water, vertical upflow, 299 data points
Yang and Webb [59]	$\left(\frac{dP}{dz}\right)_F = -0.87 Re_{eq}^{0.12} f_{fo} \frac{G_{eq}^2 v_f}{D_h}$ $Re_{eq} = \frac{G_{eq} D_h}{\mu_f}$, $G_{eq} = G\left[(1-x_e) + x_e\left(\frac{\rho_f}{\rho_g}\right)^{0.5}\right]$	Adiabatic, multi-channel (N = 4), rectangular aluminum, D_h = 1.56, 2.64 mm, R12, horizontal
Wang et al. [60]	for $G \geqslant 200$ kg/m^2 s, $\left(\frac{dP}{dz}\right)_F = \left(\frac{dP}{dz}\right)_g \phi_g^2$, $\phi_g^2 = 1 + 9.4 X^{0.62} + 0.564 X^{2.45}$ for $G < 200$ kg/m^2 s, $\left(\frac{dP}{dz}\right)_F = \left(\frac{dP}{dz}\right)_f \phi_f^2$, $\phi_f^2 = 1 + \frac{C}{X} + \frac{1}{X^2}$, $C = 4.566 \times 10^{-6} X^{0.128} Re_{fo}^{0.938}\left(\frac{v_f}{v_g}\right)^{2.15}\left(\frac{\mu_f}{\mu_g}\right)^{5.1}$	Adiabatic, circular Pyrex glass, D_h = 6.5 mm, R134a, R22, R407c, horizontal
Yan and Lin [61]	$\left(\frac{dP}{dz}\right)_F = -0.22 Re_{eq}^{-0.1} \frac{G_{eq}^2 v_f}{D_h}$	Circular copper, D_h = 2.0 mm, R134a, horizontal
Tran et al. [62]	$\left(\frac{dP}{dz}\right)_F = \left(\frac{dP}{dz}\right)_{fo} \phi_{fo}^2 \phi_{fo} = 1 + \left[4.3 \frac{(dP/dz)_{go}}{(dP/dz)_{fo}} - 1\right]\left[N_{conf} x_e^{0.875}(1-x_e)^{0.875} + x_e^{1.75}\right]$ $N_{conf} = \sqrt{\frac{\sigma}{g(\rho_f - \rho_g) D_h^2}}$	Adiabatic, circular/rectangular stainless steel, brass, D_h = 2.40, 2.46, 2.92 mm, R113, R12, R134a, horizontal
Chen et al. [63]	$\left(\frac{dP}{dz}\right)_F = \left(\frac{dP}{dz}\right)_{fo,Friedel} \times \Omega$ for $Bd^* < 2.5$, $\Omega = \frac{0.0333 Re_{fo}^{0.45}}{Re_g^{0.09}(1 + 0.4\exp(-Bd^*))}$ for $Bd^* \geqslant 2.5$, $\Omega = \frac{We_H^{0.2}}{(2.5 + 0.06 Bd^*)}$, $Bd^* = \frac{g(\rho_f - \rho_g)(D_h/2)^2}{\sigma}$	Adiabatic, circular copper, D_h = 1.02–9 mm, R410a, air–water, horizontal, 886 data points
Yu et al. [64]	$\left(\frac{dP}{dz}\right)_F = \left(\frac{dP}{dz}\right)_f \phi_f^2$, $\phi_f^2 = \left[18.65\left(\frac{\rho_g}{\rho_f}\right)^{0.5}\left(\frac{1-x_e}{x_e}\right)\frac{Re_g^{0.1}}{Re_f^{0.5}}\right]^{-1.9}$	Circular stainless steel, D_h = 2.98 mm, water, horizontal, 327 data points
	Correlations specifically developed for mini/micro-channel flows	
Lee and Lee [65]	$\left(\frac{dP}{dz}\right)_F = \left(\frac{dP}{dz}\right)_f \phi_f^2$, $\phi_f^2 = 1 + \frac{C}{X} + \frac{1}{X^2}$ $C_{vv} = 6.833 \times 10^{-8} \lambda^{-1.317} \psi^{0.719} Re_{fo}^{0.557}$, $C_{tv} = 3.627 Re_{fo}^{0.174}$ $C_{vt} = 6.185 \times 10^{-2} Re_{fo}^{0.726}$, $C_{tt} = 0.048 Re_{fo}^{0.451}$ $\psi = \frac{\mu_f j_f}{\sigma}$, $\lambda = \frac{\mu_f^2}{\rho_f \sigma D_h}$	Adiabatic, rectangular acrylic, D_h = 1.02–9 mm, air–water, horizontal, 305 data points
Hwang and Kim [66]	$\left(\frac{dP}{dz}\right)_F = \left(\frac{dP}{dz}\right)_f \phi_f^2$, $\phi_f^2 = 1 + \frac{C}{X} + \frac{1}{X^2}$ $C = 0.227 Re_{fo}^{0.452} X^{-0.32} N_{conf}^{-0.82}$	Adiabatic, circular stainless steel, D_h = 0.244, 0.430, 0.792 mm, R134a, horizontal
Sun and Mishima [67]	$\left(\frac{dP}{dz}\right)_F = \left(\frac{dP}{dz}\right)_f \phi_f^2$ for $Re_f < 2000$ and $Re_g < 2000$, $\phi_f^2 = 1 + \frac{C}{X} + \frac{1}{X^2}$, $C = 24\left(1 + \frac{Re_f}{1000}\right)\left[1 - \exp\left(\frac{-0.153}{0.27 N_{conf} + 0.8}\right)\right]$ for $Re_f \geqslant 2000$ and $Re_g \geqslant 2000$, $\phi_f^2 = 1 + \frac{C}{X^{1.19}} + \frac{1}{X^2}$, $C = 1.79\left(\frac{Re_g}{Re_f}\right)^{0.4}\left(\frac{1-x_e}{x_e}\right)^{0.5}$	Adiabatic/diabatic, circular/rectangular, D_h = 0.506–12 mm, R123, R134a, R22, R236ea, R245fa, R404a, R407C, R410a, R507, air–water, CO_2, horizontal, vertical, 2092 data points from 18 sources
Li and Wu [68]	$\left(\frac{dP}{dz}\right)_F = \left(\frac{dP}{dz}\right)_f \phi_f^2$, $\phi_f^2 = 1 + \frac{C}{X} + \frac{1}{X^2}$ for $Bd \leqslant 1.5$, $C = 11.9 Bd^{0.45}$ for $1.5 < Bd \leqslant 11$, $C = 109.4\left(Bd Re_f^{0.5}\right)^{-0.56}$ for $Bd > 11$, HEM using Beattie and Whalley [51] mixture viscosity model is recommended	Adiabatic, circular/rectangular, D_h = 0.148–3.25 mm, R12, R134a, R22, R236ea, R245fa, R32, R404a, R410a, R422d, ammonia, propane, nitrogen, horizontal, 769 data points

Table 5 (*continued*)

Author(s)	Correlation	Remarks
Zhang et al. [69]	$\left(\frac{dP}{dz}\right)_F = \left(\frac{dP}{dz}\right)_f \phi_f^2$, $\phi_f^2 = 1+\frac{C}{X}+\frac{1}{X^2}$ $C = 21[1-\exp(-0.142/N_{conf})]$	Adiabatic/diabatic, circular/rectangular, D_h = 0.07–6.25 mm, R12, R113, R22, R134a, R404a, water, ammonia, air, N_2, 2201 data points from 13 sources
Li and Wu [70]	for $Bd < 0.1$, $\left(\frac{dP}{dz}\right)_F = \left(\frac{dP}{dz}\right)_f \phi_f^2$, $\phi_f^2 = 1+\frac{C}{X}+\frac{1}{X^2}$, $C = 5.60Bd^{0.28}$ for $0.1 \leqslant Bd$ and $BdRe_f^{0.5} \leqslant 200$, $\left(\frac{dP}{dz}\right)_F = \left(\frac{dP}{dz}\right)_{fo} \phi_{fo}^2$, $\phi_{fo}^2 = (1-x_e)^2 + 2.87x_e^2 P_R^{-1} + 1.54Bd^{0.19}\left(\frac{\rho_f-\rho_g}{\rho_H}\right)^{0.81}$ for $200 < BdRe_f^{0.5}$, HEM using Beattie and Whalley [49] mixture viscosity model is recommended	Adiabatic, circular/rectangular, D_h = 0.148–3.25 mm, R12, R134a, R22, R236ea, R245fa, R32, R404a, R410a, R422d, ammonia, propane, nitrogen, horizontal, 769 data points
Kim and Mudawar [53]	$\left(\frac{dP}{dz}\right)_F = \left(\frac{dP}{dz}\right)_f \phi_f^2$, $\phi_f^2 = 1+\frac{C}{X}+\frac{1}{X^2}$, $X^2 = \frac{(dP/dz)_f}{(dP/dz)_g}$ $-\left(\frac{dP}{dz}\right)_f = \frac{2f_f v_f G^2(1-x_e)^2}{D_h}$, $-\left(\frac{dP}{dz}\right)_g = \frac{2f_g v_g G^2 x_e^2}{D_h}$ for $Re_k < 2000$, $f_k = 16Re_k^{-1}$ for circular $f_k Re_k = 24[1-1.3553\beta+1.9467\beta^2-1.7012\beta^3+0.9564\beta^4-0.2537\beta^5]$ for rectangular for $2000 \leqslant Re_k < 20,000$, $f_k = 0.079Re_k^{-0.25}$ for $20,000 \leqslant Re_k$, $f_k = 0.046Re_k^{-0.2}$ $Re_f = \frac{G(1-x)D_h}{\mu_f}$, $Re_g = \frac{GxD_h}{\mu_g}$ for $Re_f < 2000$ and $Re_g < 2000$ (vv) $C = 3.5\times10^{-5}Re_{fo}^{0.44}Su_{go}^{0.50}\left(\frac{\rho_f}{\rho_g}\right)^{0.48}\left[1+530We_{fo}^{0.52}\left(Bo\frac{P_H}{P_F}\right)^{1.09}\right]$ for $Re_f < 2000$ and $Re_g \geqslant 2000$ (vt) $C = 0.0015Re_{fo}^{0.59}Su_{go}^{0.19}\left(\frac{\rho_f}{\rho_g}\right)^{0.36}\left[1+530We_{fo}^{0.52}\left(Bo\frac{P_H}{P_F}\right)^{1.09}\right]$ for $Re_f \geqslant 2000$ and $Re_g < 2000$ (tv) $C = 8.7\times10^{-4}Re_{fo}^{0.17}Su_{go}^{0.50}\left(\frac{\rho_f}{\rho_g}\right)^{0.14}\left[1+60We_{fo}^{0.32}\left(Bo\frac{P_H}{P_F}\right)^{0.78}\right]$ for $Re_f \geqslant 2000$ and $Re_g \geqslant 2000$ (tt) $C = 0.39Re_{fo}^{0.03}Su_{go}^{0.10}\left(\frac{\rho_f}{\rho_g}\right)^{0.35}\left[1+60We_{fo}^{0.32}\left(Bo\frac{P_H}{P_F}\right)^{0.78}\right]$ $Re_{fo} = \frac{GD_h}{\mu_f}$, $Su_{go} = \frac{\rho_g \sigma D_h}{\mu_g^2}$, $We_{fo} = \frac{G^2 D_h}{\rho_f \sigma}$, $Bo = \frac{q''_H}{G h_{fg}}$	Adiabatic/diabatic, circular/rectangular, D_h = 0.349–5.35 mm, R12, R134a, R245fa, R410a, FC72, ammonia, CO_2, water, horizontal, vertical, 2378 data points from 16 sources

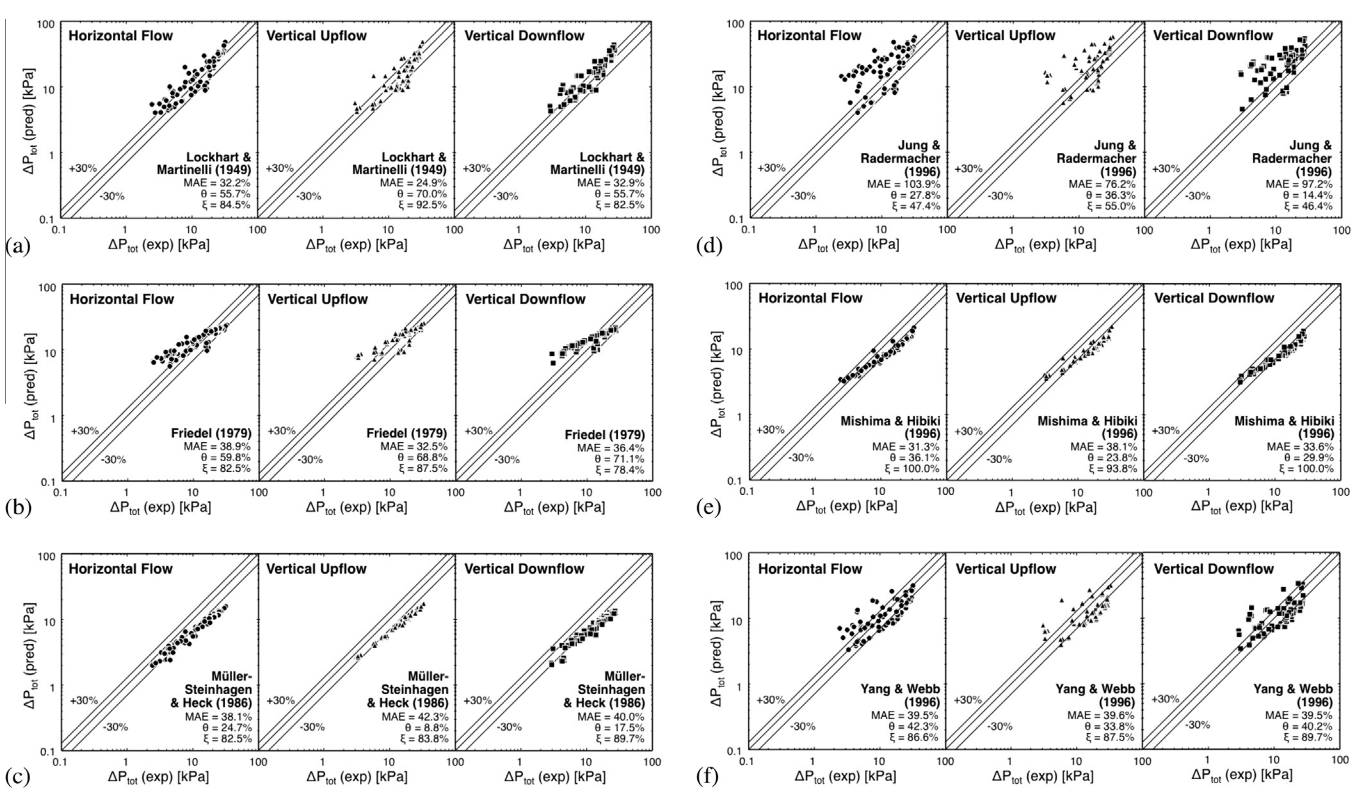

Fig. 8. Comparison of measured total pressure drop for horizontal flow, vertical upflow and vertical downflow with predictions of Separated Flow Models (*SFMs*) by (a) Lockhart and Martinelli [54], (b) Friedel [55], and (c) Müller-Steinhagen and Heck [56], (d) Jung and Radermacher [57], (e) Mishima and Hibiki [58], and (f) Yang and Webb [59].

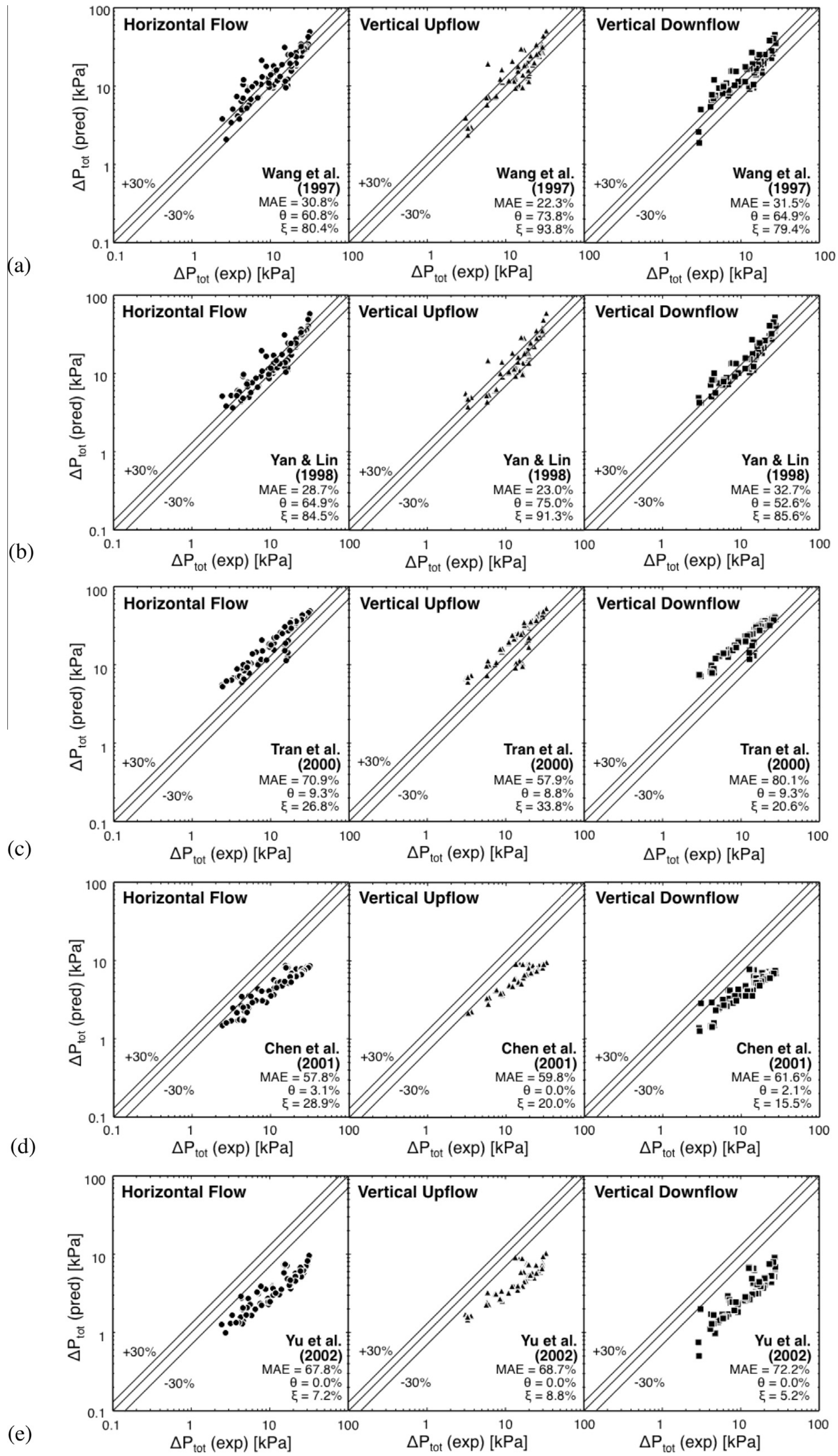

Fig. 9. Comparison of measured total pressure drop for horizontal flow, vertical upflow and vertical downflow with predictions of Separated Flow Models (*SFMs*) by (a) Wang et al. [60], (b) Yan and Lin [61], (c) Tran et al. [62], (d) Chen et al. [63], and (e) Yu et al. [64].

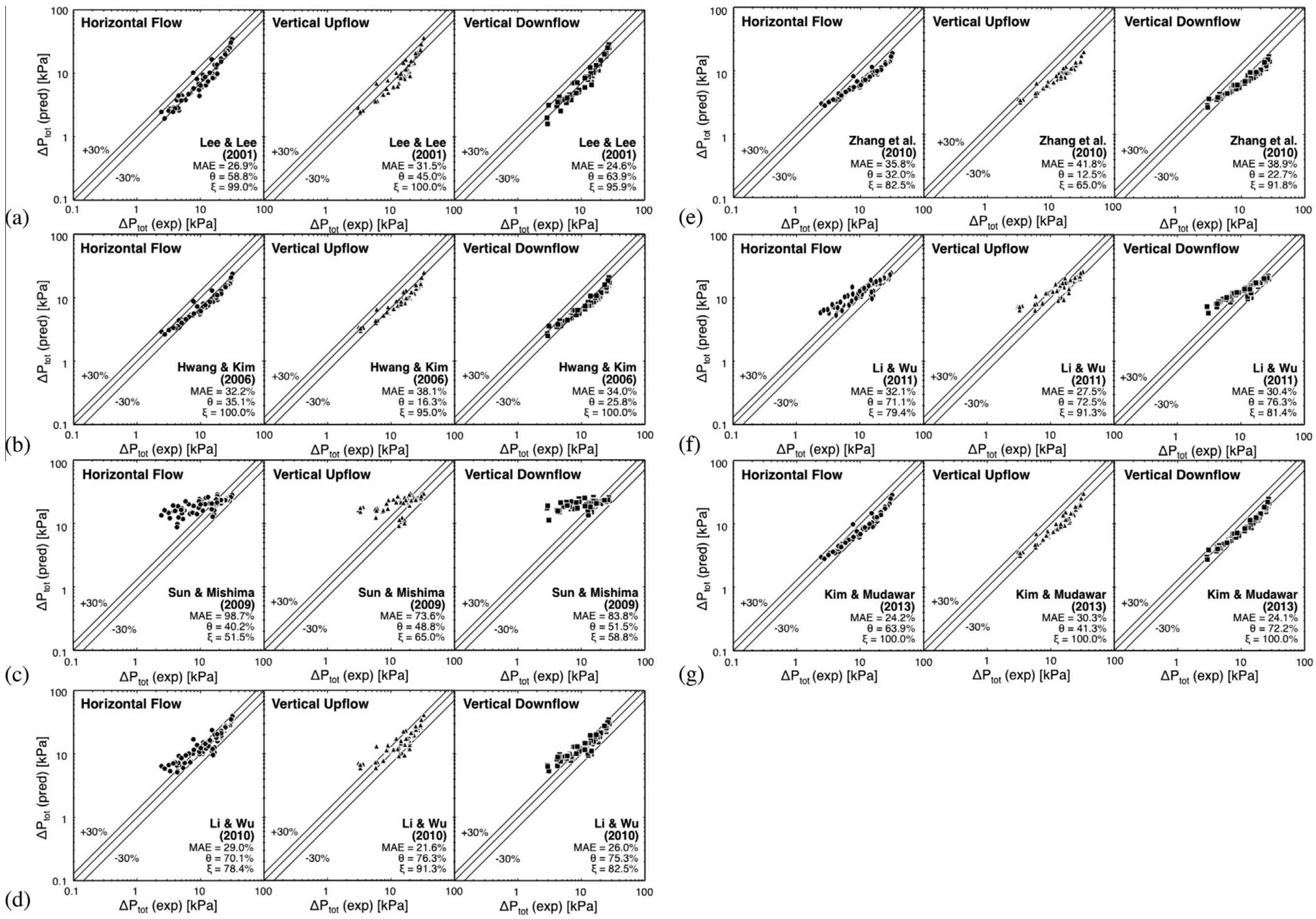

Fig. 10. Comparison of measured total pressure drop for horizontal flow, vertical upflow and vertical downflow with predictions of mini/micro-channel Separated Flow Models (*SFMs*) by (a) Lee and Lee [65], (b) Hwang and Kim [66], (c) Sun and Mishima [67], (d) Li and Wu [68], (e) Zhang et al. [69], (f) Li and Wu [70], and (g) Kim and Mudawar [53].

Both criteria must be tested simultaneously to determine the corresponding range for G/ρ_f; the dominant criterion for specific operating conditions is the one that yields the larger G/ρ_f value. Eqs. (16) and (17) can also be used to determine G/ρ_f for say Lunar gravity ($0.17g_e$) or Martian gravity ($0.38g_e$). Using these two equations for Earth gravity yields $G/\rho_f \geqslant 0.98$ m/s and $G/\rho_f \geqslant 0.43$ m/s, respectively. Therefore, gravitational effects for macro-channel flow can be eliminated with $G/\rho_f \geqslant 0.98$ m/s.

As shown in Fig. 5g of part 1 of this study [25], orientation effects are negated altogether for the present micro-channel flow with $G/\rho_f \geqslant 0.22$ m/s, which is significantly smaller than the value of 0.98 m/s required for macro-channels. This demonstrates the superiority of micro-channels at negating body force effects for space systems compared to macro-channels. In effect, the Bo/We^2 and $1/Fr$ criteria given by Eqs. (16) and (17) provide a high upper limit for the value of G/ρ_f required to negate body force effects.

Therefore, using the predictive tools presented above, optimum design of a micro-channel evaporator for a space vehicle can be achieved through a trade study aimed at simultaneously (1) reducing pressure drop, (2) maintaining heat flux safely below CHF, and (3) negating the influence of body force.

5. Conclusions

Using data for pressure drop and heat transfer coefficient for flow boiling in micro-channels at different orientations from part 1 [25], the present part of a two-part study examined the accuracy of published predictive tools. Also examined is the effectiveness of micro-channels at negating the influence of body force in reduced gravity space systems. Key findings from the study are as follows:

(1) The two-phase heat transfer coefficient data are compared with predictions of 15 popular correlations. These correlations are grouped into three distinct types: (i) correlations based on nucleate boiling (*nb*) or convective boiling (*cb*) relations, (ii) correlations based on maximum value predicted using *nb* and *cb* relations, and (iii) correlations involving superpositioning of *nb* and *cb* relations. Overall, correlations of the first type show poor predictions, with the exception of Agostini and Bontemps' [31], which yields MAEs of 17.2%, 16.1%, and 13.4%, for horizontal flow, vertical upflow, and vertical downflow, respectively. Correlations of the second type provide fair accuracy, but with appreciable scatter. And correlations of the third type generally provide fair to good predictions, with Kim and Mudawar's [42] yielding the best predictions, with MAEs of 19.0%, 19.9% and 16.9% for horizontal flow, vertical upflow and vertical downflow, respectively.

(2) The pressure drop data are compared with the predictions of the Homogeneous Equilibrium Model (*HEM*) in conjunction with 7 mixture viscosity relations, and 18 Separate Flow Models (*SFMs*). Using the *HEM*, the relation by Lin et al. [52] shows the best accuracy of all 7 mixture viscosity relations, with MAEs of 22.0%, 28.9% and 22.8% for horizontal

flow, vertical upflow and vertical downflow, respectively. Of the 18 *SFM*-based correlations, Kim and Mudawar's [53] shows the best accuracy, with MAEs of 24.2%, 30.3% and 24.1% for horizontal flow, vertical upflow and vertical downflow, respectively.

(3) Three important criteria for implementing micro-channel flow boiling in space systems are proposed: (i) avoiding large pressure drop, (ii) avoiding critical heat flux (CHF), and (iii) negating the influence of body force. By requiring sigificantly smaller mass velocities to negate body force effects, it is shown that micro-channels are far more effective for space applications than macro-channels.

Conflict of interest

None declared.

Acknowledgement

The authors are grateful for the support of the National Aeronautics and Space Administration (NASA) – United States under Grant No. NNX13AC83G.

References

[1] I. Mudawar, Two-phase micro-channel heat sinks: theory, applications an limitations, J. Electron. Pack. – Trans. ASME 133 (2011) 041002.

[2] D.B. Tuckerman, R.F.W. Pease, High-performance heat sinking for VLSI, Electron. Dev. Lett. – Trans. IEEE 2 (1981) 126–129.

[3] A.G. Fedorov, R. Viskanta, Three-dimensional conjugate heat transfer in the microchannel heat sink for electronic packaging, Int. J. Heat Mass Transfer 43 (2000) 399–415.

[4] W. Qu, I. Mudawar, Experimental and numerical study of pressure drop and heat transfer in a single-phase micro-channel heat sink, Int. J. Heat Mass Transfer 45 (2000) 2549–2565.

[5] M.K. Sung, I. Mudawar, Experimental and numerical investigation of single-phase heat transfer using a hybrid jet-impingement/micro-channel cooling scheme, Int. J. Heat Mass Transfer 49 (2006) 682–694.

[6] M.K. Sung, I. Mudawar, Single-phase hybrid micro-channel/jet impingement cooling, Int. J. Heat Mass Transfer 51 (2008) 4342–4352.

[7] C.Y. Han, P. Griffith, The mechanism of heat transfer in nucleate pool boiling, Int. J. Heat Mass Transfer 8 (1965) 887–903.

[8] P.J. Marto, V.J. Lepere, Pool boiling heat transfer from enhanced surfaces to dielectric fluids, J. Heat Transfer – Trans. ASME 104 (1982) 292–299.

[9] T.M. Anderson, I. Mudawar, Microelectronic cooling by enhanced pool boiling of a dielectric fluorocarbon liquid, J. Heat Transfer – Trans. ASME 111 (1989) 752–759.

[10] I. Mudawar, A.H. Howard, C.O. Gersey, An analytical model for near-saturated pool boiling CHF on vertical surfaces, Int. J. Heat Mass Transfer 40 (1997) 2327–2339.

[11] S. Yilmaz, J.W. Westwater, Effect of velocity on heat transfer in boiling Freon-l 13, J. Heat Transfer 102 (1) (1980) 26–31.

[12] Y. Katto, Critical heat flux, Adv. Heat Transfer 17 (1985) 1–64.

[13] T.C. Willingham, I. Mudawar, Forced-convection boiling and critical heat flux from a linear array of discrete heat sources, Int. J. Heat Mass Transfer 35 (1992) 2879–2890.

[14] Y. Katto, M. Kunihiro, Study of the mechanism of burn-out in boiling system of high burn-out heat flux, Bull. JSME 16 (1973) 1357–1366.

[15] M. Monde, T. Inoue, Critical heat flux in saturated forced convective boiling on a heated disk with multiple impinging jets, J. Heat Transfer – Trans. ASME 113 (1991) 722–727.

[16] D.C. Wadsworth, I. Mudawar, Enhancement of single-phase heat transfer and critical heat flux from an ultra-high-flux-source to a rectangular impinging jet of dielectric liquid, J. Heat Transfer – Trans. ASME 114 (1992) 764–768.

[17] M.E. Johns, I. Mudawar, An ultra-high power two-phase jet-impingement avionic clamshell module, J. Electron. Pack. – Trans. ASME 118 (1996) 264–270.

[18] S. Toda, A study in mist cooling (1st report: investigation of mist cooling), Trans. JSME 38 (1972) (1972) 581–588.

[19] L. Lin, R. Ponnappan, Heat transfer characteristics of spray cooling in a closed loop, Int. J. Heat Mass Transfer 46 (2003) 3737–3746.

[20] J.R. Rybicki, I. Mudawar, Single-phase and two-phase cooling characteristics of upward-facing and downward-facing sprays, Int. J. Heat Mass Transfer 49 (2006) 5–16.

[21] M. Visaria, I. Mudawar, Theoretical and experimental study of the effects of spray orientation on two-phase spray cooling and critical heat flux, Int. J. Heat Mass Transfer 51 (2008) 2398–2410.

[22] W. Nakayama, T. Nakajima, S. Hirasawa, Heat sink studs having enhanced boiling surfaces for cooling of microelectronic components, ASME Paper 84-WA/HT-89, 1984.

[23] R.L. Webb, The evolution of enhanced surface geometries for nucleate boiling, Heat Transfer Eng. 2 (1981) 46–69.

[24] V. Khanikar, I. Mudawar, T. Fisher, Effects of carbon nanotube coating on flow boiling in a micro-channel, Int. J. Heat Mass Transfer 52 (2009) 3805–3817.

[25] H. Lee, I. Park, I. Mudawar, M.M. Hasan, Micro-channel evaporator for space applications – 1. Experimental pressure drop and heat transfer results for different orientations in Earth gravity, Int. J. Heat Mass Transfer (2014), http://dx.doi.org/10.1016/j.ijheatmasstransfer.2014.06.012.

[26] G.M. Lazarek, S.H. Black, Evaporative heat transfer, pressure drop and critical heat flux in a small vertical tube with R-113, Int. J. Heat Mass Transfer 25 (1982) 945–960.

[27] M.G. Cooper, Saturation nucleate pool boiling – a simple correlation, Ind. Chem. Eng. Symp. Ser. 86 (1984) 785–793.

[28] T.N. Tran, M.W. Wambsganss, D.M. France, Small circular- and rectangular channel boiling with two refrigerants, Int. J. Multiphase Flow 22 (1996) 485–498.

[29] H.J. Lee, S.Y. Lee, Heat transfer correlation for boiling flows in small rectangular horizontal channels with low aspect ratios, Int. J. Multiphase Flow 27 (2001) 2043–2062.

[30] G.R. Warrier, V.K. Dhir, L.A. Momoda, Heat transfer and pressure drop in narrow rectangular channels, Exp. Therm. Fluid Sci. 26 (2002) 53–64.

[31] B. Agostini, A. Bontemps, Vertical flow boiling of refrigerant R134a in small channels, Int. J. Heat Fluid Flow 26 (2005) 296–306.

[32] W. Li, Z. Wu, A general correlation for evaporative heat transfer in micro/minichannels, Int. J. Heat Mass Transfer 53 (2010) 1778–1787.

[33] H.K. Oh, C.H. Son, Flow boiling heat transfer and pressure drop characteristics of CO_2 in horizontal tube of 4.57-mm inner diameter, Appl. Therm. Eng. 31 (2011) 163–172.

[34] M.M. Shah, A new correlation for heat transfer during boiling flow through pipes, ASHRAE Trans. 82 (1976) 66–86.

[35] M.M. Shah, Chart correlation for saturated boiling heat transfer: equations and further study, ASHRAE Trans. 88 (1982) 185–196.

[36] M. Ducoulombier, S. Colasson, J. Bonjour, P. Haberschill, Carbon dioxide flow boiling in a single microchannel – Part II: Heat transfer, Exp. Therm. Fluid Sci. 35 (2011) 597–611.

[37] J.C. Chen, Correlation for boiling heat transfer to saturated fluids in convective flow, Ind. Eng. Chem. Process Des. Dev. 5 (1966) 322–329.

[38] S. Edelstein, A.J. Perez, J.C. Chen, Analytic representation of convective boiling functions, AIChE J. 30 (1984) 840–841.

[39] K.E. Gungor, R.H.S. Winterton, A general correlation for flow boiling in tubes and annuli, Int. J. Heat Mass Transfer 29 (1986) 351–358.

[40] Z. Liu, R.H.S. Winterton, A general correlation for saturated and subcooled flow boiling in tubes and annuli, based on a nucleate pool boiling equation, Int. J. Heat Mass Transfer 34 (1991) 2759–2766.

[41] S.S. Bertsch, E.A. Groll, S.V. Garimella, A composite heat transfer correlation for saturated flow boiling in small channels, Int. J. Heat Mass Transfer 52 (2009) 2110–2118.

[42] S.M. Kim, I. Mudawar, Universal approach to predicting saturated flow boiling heat transfer in mini/micro-channels – Part II. Two-phase heat transfer coefficient, Int. J. Heat Mass Transfer 64 (2013) 1239–1256.

[43] R.K. Shah, A.L. London, Laminar flow forced convection in ducts: a source book for compact heat exchanger analytical data – Suppl. 1, Academic Press, New York, 1978.

[44] S.M. Kim, I. Mudawar, Consolidated method to predicting pressure drop and heat transfer coefficient for both subcooled and saturated flow boiling in micro-channel heat sinks, Int. J. Heat Mass Transfer 55 (2012) 3720–3731.

[45] S.M. Zivi, Estimation of steady-state steam void-fraction by means of the principle of minimum entropy production, J. Heat Transfer – Trans. ASME 86 (1964) 247–252.

[46] W.H. McAdams, W.K. Woods, L.C. Heroman, Vaporization inside horizontal tubes, II. Benzene–oil mixture, Trans. ASME 64 (1942) 193–200.

[47] W.W. Akers, H.A. Deans, O.K. Crosser, Condensing heat transfer within horizontal tubes, Chem. Eng. Prog. 54 (1958) 89–90.

[48] A. Cicchitti, C. Lombardi, M. Silvestri, G. Soldaini, R. Zavalluilli, Two-phase cooling experiments-pressure drop, heat transfer and burnout measurements, Energia Nucl. 7 (1960) 407–425.

[49] W.L. Owens, Two-phase pressure gradient, in: Int. Dev. Heat Transfer, Part II, ASME, New York, 1961.

[50] A.E. Dukler, M. Wicks, R.G. Cleaveland, Pressure drop and hold up in two-phase flow, AIChE J. 10 (1964) 38–51.

[51] D.R.H. Beattie, P.B. Whalley, A simple two-phase frictional pressure drop calculation method, Int. J. Multiphase Flow 8 (1982) 83–87.

[52] S. Lin, C.C.K. Kwok, R.Y. Li, Z.H. Chen, Z.Y. Chen, Local frictional pressure drop during vaporization of R-12 through capillary tubes, Int. J. Multiphase Flow 17 (1991) 95–102.

[53] S.M. Kim, I. Mudawar, Universal approach to predicting two-phase frictional pressure drop for mini/micro-channel saturated flow boiling, Int. J. Heat Mass Transfer 58 (2013) 718–734.

[54] R.W. Lockhart, R.C. Martinelli, Proposed correlation of data for isothermal two-phase, two-component flow in pipes, Chem. Eng. Prog. 45 (1949) 39–48.

[55] L. Friedel, Improved friction pressure drop correlations for horizontal and vertical two-phase pipe flow, in: European Two-Phase Group Meeting, Ispra, Italy, 1979, Paper E2.

[56] H. Müller-Steinhagen, K. Heck, A simple friction pressure drop correlation for two-phase flow in pipes, Chem. Eng. Process 20 (1986) 297–308.
[57] D.S. Jung, R. Radermacher, Prediction of pressure drop during horizontal annular flow boiling of pure and mixed refrigerants, Int. J. Heat Mass Transfer 32 (1989) 2435–2446.
[58] K. Mishima, T. Hibiki, Some characteristics of air–water two-phase flow in small diameter vertical tubes, Int. J. Multiphase Flow 22 (1996) 703–712.
[59] C.Y. Yang, R.L. Webb, Friction pressure drop of R-12 in small hydraulic diameter extruded aluminum tubes with and without micro-fins, Int. J. Heat Mass Transfer 39 (1996) 801–809.
[60] C.C. Wang, C.S. Chiang, D.C. Lu, Visual observation of two-phase flow pattern of R-22, R-134a, and R-407C in a 6.5-mm smooth tube, Exp. Therm. Fluid Sci. 15 (1997) 395–405.
[61] Y.Y. Yan, T.F. Lin, Evaporation heat transfer and pressure drop of refrigerant R-134a in a small pipe, Int. J. Heat Mass Transfer 41 (1998) 4183–4194.
[62] T.N. Tran, M.C. Chyu, M.W. Wambsganss, D.M. France, Two-phase pressure drop of refrigerants during flow boiling in small channels: an experimental investigation and correlation development, Int. J. Multiphase Flow 26 (2000) 1739–1754.
[63] I.Y. Chen, K.S. Yang, Y.J. Chang, C.C. Wang, Two-phase pressure drop of air–water and R-410A in small horizontal tubes, Int. J. Multiphase Flow 27 (2001) 1293–1299.
[64] W. Yu, D.M. France, M.W. Wambsganss, J.R. Hull, Two-phase pressure drop, boiling heat transfer, and critical heat flux to water in a small-diameter horizontal tube, Int. J. Multiphase Flow 28 (2002) 927–941.
[65] H.J. Lee, S.Y. Lee, Pressure drop correlations for two-phase flow within horizontal rectangular channels with small heights, Int. J. Multiphase Flow 27 (2001) 783–796.
[66] Y.W. Hwang, M.S. Kim, The pressure drop in microtubes and the correlation development, Int. J. Heat Mass Transfer 49 (2006) 1804–1812.
[67] L. Sun, K. Mishima, Evaluation analysis of prediction methods for two-phase flow pressure drop in mini-channels, Int. J. Multiphase Flow 35 (2009) 47–54.
[68] W. Li, Z. Wu, A general correlation for adiabatic two-phase pressure drop in micro/mini-channels, Int. J. Heat Mass Transfer 53 (2010) 2732–2739.
[69] W. Zhang, T. Hibiki, K. Mishima, Correlations of two-phase frictional pressure drop and void fraction in mini-channel, Int. J. Heat Mass Transfer 53 (2010) 453–465.
[70] W. Li, Z. Wu, Generalized adiabatic pressure drop correlations in evaporative micro/mini-channels, Exp. Therm. Fluid Sci. 35 (2011) 866–872.
[71] H. Zhang, I. Mudawar, M.M. Hasan, Experimental and theoretical study of orientation effects on flow boiling CHF, Int. J. Heat Mass Transfer 45 (2002) 4463–4477.
[72] H. Zhang, I. Mudawar, M.M. Hasan, A method for assessing the importance of body force on flow boiling CHF, J. Heat Transfer – Trans. ASME 126 (2004) 161–168.
[73] C.R. Kharangate, I. Mudawar, M.H. Hasan, Experimental and theoretical study of critical heat flux in vertical upflow with inlet vapor void, Int. J. Heat Mass Transfer 55 (2012) 360–374.
[74] C.R. Kharangate, I. Mudawar, M.H. Hasan, Photographic study and modeling of critical heat flux in horizontal flow boiling with inlet vapor void, Int. J. Heat Mass Transfer 55 (2012) 4154–4168.
[75] C. Konishi, I. Mudawar, M.H. Hasan, Investigation of the influence of orientation on critical heat flux for flow boiling with two-phase inlet, Int. J. Heat Mass Transfer 61 (2013) 176–190.
[76] C. Konishi, I. Mudawar, M.H. Hasan, Criteria for negating the influence of gravity on flow boiling critical heat flux with two-phase inlet conditions, Int. J. Heat Mass Transfer 65 (2013) 203–218.
[77] H. Zhang, I. Mudawar, M.M. Hasan, Flow boiling CHF in microgravity, Int. J. Heat Mass Transfer 48 (2005) 3107–3118.
[78] H. Zhang, I. Mudawar, M.M. Hasan, CHF model for subcooled flow boiling in Earth gravity and microgravity, Int. J. Heat Mass Transfer 50 (2007) 4039–4051.